MICROBIOLOGY

Commensal microbiome promotes hair follicle regeneration by inducing keratinocyte HIF-1α signaling and glutamine metabolism

Gaofeng Wang[1,2]*, Evan Sweren[2], William Andrews[3], Yue Li[1], Junjun Chen[2], Yingchao Xue[2], Eric Wier[2], Martin P. Alphonse[2], Li Luo[4], Yong Miao[1], Ruosi Chen[1,2], Dongqiang Zeng[5], Sam Lee[2], Ang Li[2], Erika Dare[2], Dongwon Kim[2,6], Nathan K. Archer[2], Sashank K. Reddy[2,7], Linda Resar[4], Zhiqi Hu[1], Elizabeth A. Grice[8], Maureen A. Kane[3], Luis A. Garza[2,9,10]*

Tissue injury induces metabolic changes in stem cells, which likely modulate regeneration. Using a model of organ regeneration called wound-induced hair follicle neogenesis (WIHN), we identified skin-resident bacteria as key modulators of keratinocyte metabolism, demonstrating a positive correlation between bacterial load, glutamine metabolism, and regeneration. Specifically, through comprehensive multiomic analysis and single-cell RNA sequencing in murine skin, we show that bacterially induced hypoxia drives increased glutamine metabolism in keratinocytes with attendant enhancement of skin and hair follicle regeneration. In human skin wounds, topical broad-spectrum antibiotics inhibit glutamine production and are partially responsible for reduced healing. These findings reveal a conserved and coherent physiologic context in which bacterially induced metabolic changes improve the tolerance of stem cells to damage and enhance regenerative capacity. This unexpected proregenerative modulation of metabolism by the skin microbiome in both mice and humans suggests important methods for enhancing regeneration after injury.

INTRODUCTION

The microbiome plays an important role in homeostatic tissue maintenance, healing, and regeneration (*1*–*3*). Studies have shown that in pathologic conditions and trauma, commensal microbiomes alter host metabolisms (*4*, *5*). For example, when exposed to ionizing radiation, the intestinal bacteria *Lachnospiraceae* and *Enterococcaceae* can promote propionate and tryptophan metabolism, improving host hematopoiesis and repairing intestinal damage (*6*). Likewise, in transplant studies, the intestinal microbiome of young mice enhances the intestinal health of old recipient mice through increased *Firmicutes* and *Lachnospiraceae* and the promotion of butyrate metabolism (*7*). In the skin, cutaneous microbes are also essential for the host's metabolic regulation (*8*, *9*). However, the microbiome's effect on metabolic function during injury repair has been less well studied.

We have previously shown that the commensal microbiome has a positive effect on skin regeneration, specifically through interleukin-1β (IL-1β) signaling (*1*). When skin injury induces inflammation, immune cells—mainly macrophages—release IL-1β to stimulate wound-induced hair follicle neogenesis (WIHN). Keratinocytes also express high levels of IL-1β in inflammatory skin diseases or trauma (*10*, *11*). However, the mechanism by which keratinocytes generate IL-1β in these varied conditions is unknown, and it is also unclear whether metabolic alterations might be responsible.

Glutamine is an important metabolite for the transcription and production of IL-1β, as previous studies on energy metabolism have shown (*12*, *13*). Furthermore, glutamine metabolism modulated by mammalian target of rapamycin complex 2 (mTORC2) is important for repopulating hair follicle stem cells (HFSCs) after mobilization at the onset of anagen (*14*). Similarly, previous studies have shown that glutamine is an important energy source for hair follicles (*15*). Thus, glutamine metabolism might sit at the nexus of hair follicle regeneration by promoting the production of hair follicle neogenic signals and by directly activating HFSCs. However, there is ambiguity as to whether glutamine has more proinflammatory or anti-inflammatory effects (*16*–*18*). Similarly, the precise mechanisms between the microbiome, glutamine, and regeneration after injury are not yet known.

We hypothesized that skin-resident bacteria may link glutamine to skin and hair follicle regeneration by producing local hypoxia in wounds. For example, *Staphylococcus aureus* induces keratinocyte IL-1β production by hypoxia-inducible factor-1α (HIF-1α) signaling (*19*). The HIF-1α signal plays an important regulatory role in tissue hypoxia to maintain the homeostasis of the microenvironment, especially in the regulation of energy metabolism (*20*, *21*). Local oxygen concentration can directly affect the self-renewal and differentiation of stem cells. Hematopoietic stem cells, neural stem cells, and human placental cytotrophoblast cells benefit from living in a low-oxygen environment (*22*, *23*). Hypoxia promotes

[1]Department of Plastic and Aesthetic Surgery, Nanfang Hospital of Southern Medical University, Guangzhou, Guangdong Province 510515, China. [2]Department of Dermatology, Johns Hopkins University School of Medicine, Baltimore, MD 21210, USA. [3]Department of Pharmaceutical Sciences, School of Pharmacy Mass Spectrometry Center, University of Maryland, Baltimore, MD 21201, USA. [4]Departments of Medicine, Oncology, Pathology and Institute for Cellular Engineering, Johns Hopkins University School of Medicine, Baltimore, MD 21210, USA. [5]Department of Oncology, Nanfang Hospital of Southern Medical University, Guangzhou, Guangdong Province 510515, China. [6]Department of Bio-Chemical Engineering, Dongseo University, Busan, Republic of Korea. [7]Department of Plastic and Reconstructive Surgery, Johns Hopkins School of Medicine, Baltimore, MD 21287, USA. [8]Department of Dermatology and Microbiology, Perelman School of Medicine, University of Pennsylvania, Philadelphia, PA 19104, USA. [9]Department of Cell Biology, Johns Hopkins University School of Medicine, Baltimore, MD 21210, USA. [10]Department of Oncology, Johns Hopkins University School of Medicine, Baltimore, MD 21210, USA.
*Corresponding author. Email: gwang45@jhmi.edu (G.W.); LAG@jhmi.edu (L.A.G.)

long-term preservation and maintenance of stem cells, including HFSCs (*14*, *24*). During the course of proliferation and metabolic activity, *S. aureus* contributes to hypoxia by consuming nutrients and oxygen in the microenvironment (*25*), suggesting a path through which skin flora may regulate metabolism to promote regeneration.

Our aim was to unify these disparate unconnected elements into a coherent physiologic model that tests the role of metabolism in the microbiome promotion of regeneration in mice and humans. To do so, we used spatial metabolomics and bioinformatics to systematically screen the wound microenvironment under different bacterial loads. We showed that glutamine metabolism positively correlates with bacterial load. We also demonstrated that *S. aureus* activate HIF-1α signaling by inducing tissue hypoxia, with concomitant increase in keratinocyte glutamine metabolism and production of IL-1β to promote regeneration. Furthermore, the reduction of commensal bacteria reduces glutamine levels and retards wound healing in human subjects. In aggregate, these unappreciated findings point to a conserved proregenerative metabolic program induced by skin flora with important therapeutic implications.

RESULTS

Bacteria stimulate WIHN through keratinocyte-dependent IL-1β–MyD88

Our previous study used six skin microbial gradient models to show that skin microbes promote WIHN. By screening five top mouse skin commensal microbes, we found that *S. aureus* had the strongest ability to promote WIHN; therefore, we used *S. aureus* as a representative of commensal microbes to further research mechanism (*1*). Bacterial load correlates in a dose-responsive manner to WIHN. Compared to standard laboratory specific pathogen–free (SPF) mice, germ-free (GF) mice have lower WIHN (fold change = −21.7, $P = 5.8 \times 10^{-8}$), while SPF mice treated with *S. aureus* have higher WIHN (fold change = 3.5, $P = 2.1 \times 10^{-7}$) (fig. S1A). Taxonomy analysis verified that the relative abundance of bacteria in the wound beds of GF, SPF, and *S. aureus*–treated mice increased, respectively, and significantly (fig. S1C). Unlike in SPF control mice, *Staphylococcus* was the most common bacterial strain in *S. aureus*–treated mice, with the percentages of other bacteria mostly lower than in SPF mice, showing that exogenous *S. aureus* suppresses other bacteria (fig. S1D) (*1*). In *S. aureus*–treated wounds, β-catenin and Krt15—markers of hair follicle regeneration and HFSCs, respectively—were markedly increased at scab detachment day 0 (SD0), the time when hair follicle regeneration begins (fig. S1B). We also confirmed that *Il-1*$\beta^{-/-}$ mice regenerate poorly (fold change = −42.6, $P = 2.1 \times 10^{-7}$), and this could not be rescued by *S. aureus* treatment (fig. S1, G and H). Last, we validated our previous findings that *K14-Myd88*$^{-/-}$ mice exhibit significantly lower regeneration than wild-type (WT) mice (fold change = −3.9, $P = 1.0 \times 10^{-4}$) and are likewise unresponsive to *S. aureus* rescue (fig. S1, I and J). Taxonomy analysis showed that the relative abundance of bacteria in the wound bed of *K14-Myd88*$^{-/-}$ and *Il-1*$\beta^{-/-}$ mice was significantly lower than that in WT mice, suggesting an interesting host-commensal cross-talk (fig. S1E). *Staphylococcus* was significantly higher in the WT mouse wound bed, whereas *Pseudomonas* was the dominant bacteria in the wound beds of *K14-Myd88*$^{-/-}$ and *Il-1*$\beta^{-/-}$ mice (fig. S1F). Together, these results confirm that the skin microbiome induces WIHN through keratinocyte-dependent IL-1β–Myd88 signals.

Bacteria induce keratinocyte IL-1β production via glutamine metabolism

Our next goal was to understand how bacteria induce IL-1β to promote regeneration. A previous study showed that different types of bacteria promote hair follicle regeneration in a Toll-like receptor 2/3 (TLR2/3)–independent mechanism, indicating that bacteria might promote regeneration through nonspecific pathways rather than through pattern recognition receptors. One possibility is that the microbiome may regulate metabolism in the microenvironment to promote IL-1β signaling (*8*, *9*). To explore this, we examined the energy metabolism of fatty acids, glucose, glycan, pyruvate, glutamine, and glutamate using transcriptome Gene Ontology (GO) to calculate different metabolic scores in the wounds of mice with different microbial loads (Fig. 1A). The most significantly up-regulated metabolic pathway was glutamine metabolism, which increased with bacterial load. Notably, the increase in glutamine metabolism correlated with regenerative capacity in SPF (high WIHN) mice versus GF (low WIHN) and *S. aureus* (high WIHN) versus phosphate-buffered saline (PBS) (low WIHN) mice (Fig. 1A). Because a recent study has shown that glutamine metabolism activates HFSCs and promotes the anagen phase in hair follicles, we compared glutamine and glutamate metabolic gene expression in the two above contexts, plus a third from a published literature: low (C57Bl/6J) versus high (B6/FVB/SJL) WIHN in untreated WT mice (different mouse strains) (*14*, *26*). Most of the glutamine and glutamate genes, especially glutaminase (*Gls*), were more highly expressed in high WIHN mice and positively correlated with the skin bacterial load (Fig. 1B). The expression levels of *Gls* and *Gls2* were elevated in the high WIHN group (Fig. 1C). Gene set enrichment analysis (GSEA) also confirmed that glutamine and glutamate metabolism were highly expressed in the wounded skin of mice with high bacterial loads and high regeneration (Fig. 1, D and E).

Using mass spectrometry imaging (MSI) of the spatial metabolome to visualize the expression of different metabolites, we found that the trace amines, cholesterol, and triacylglycerol did not increase significantly compared to their levels in unwounded skin (baseline), during wounding [wound day 5 (WD5)] or at the beginning of hair regeneration (SD0; fig. S2, A to C). On the basis of the previous studies, we measured metabolites that promote hair follicle growth, including gallic acid, α-ketoglutarate, inosine, inosine monophosphate, spermidine, and spermine (*27*–*30*). Likewise, we found that these metabolites did not exhibit a significantly consistent trend with the bacterial load of the skin at any tested time point (fig. S3, A to F). However, both glutamine and glutamate levels were greater in mice with high bacterial load and high WIHN during WD5 and SD0 (Fig. 1F and figs. S1K and S4A). However, there was no significant difference in glutamine and glutamate levels between high and low bacterial loads in the baseline (fig. S5, A and B). These data suggest that bacteria induce glutamine metabolism in keratinocytes during wounding. To confirm, we also collected mouse wound proteins at the start of hair follicle regeneration and detected by enzyme-linked immunosorbent assay (ELISA) that glutamate was highly expressed in high-WIHN mice (Fig. 2A).

To determine whether glutamine metabolism affects IL-1β expression in keratinocytes, thereby promoting regeneration, we

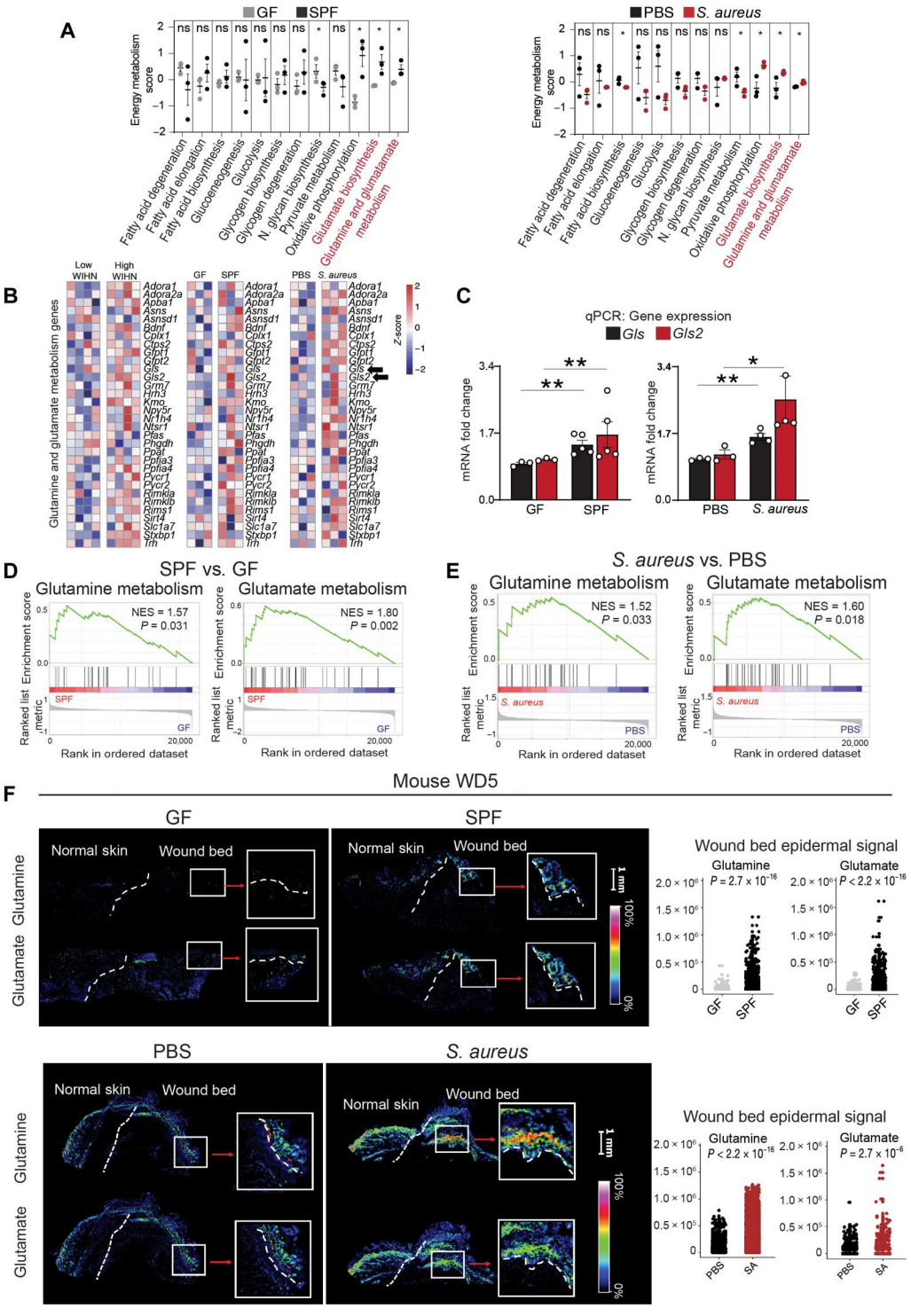

Fig. 1. Bacteria induce wound bed glutamine metabolism. (**A**) Energy metabolism score, calculated from microarray by principal components analysis (PCA) method, of GF (low WIHN) versus SPF (high WIHN) and PBS-treated (50 μl of WD3; low WIHN) versus *S. aureus*–treated mice (1×10^7 colony-forming units on WD3; high WIHN) using WD14 wound beds, the day of scab detachment (SD0). (**B**) Glutamine and glutamate gene signatures of microarrays from SD0 wound bed tissue of low WIHN strain (C57BL/6) versus high WIHN strain (B6/FVB/SJL) mice; GF versus SPF mice, and PBS-treated versus *S. aureus*–treated mice are shown. (**C**) mRNA expression of *Gls* and *Gls2* in mice SD0 wound beds as detected by quantitative reverse transcription polymerase chain reaction (qRT-PCR). (**D** and **E**) GSEA of GF, SPF, PBS-treated, and *S. aureus*–treated mice glutamine and glutamate signatures based on SD0 microarrays. (**F**) On WD5 and SD0, glutamine and glutamate metabolite abundance in wound bed tissues as detected by mass spectrometry imaging (MSI; left) and quantification (right) of GF, SPF, PBS-treated, and *S. aureus*–treated mice. The magnified images indicate the wound bed, and the white dotted lines indicate the epidermal basement membrane. In quantification, each dot represents the expression of glutamine and glutamate as measured by mass spectrometry. Scatterplots and histogram graphs indicated means ± SEM; unpaired Student's *t* test was used to compare statistical difference. $n = 3$ to 4 independent animals per group. SA, *S. aureus*.NES, normalized enrichment score.

isolated, cultured, and treated mouse keratinocytes with glutamine. We found that glutamine promoted *Il-1*β mRNA expression in keratinocytes (Fig. 2B). Keratinocytes treated with the glutaminase inhibitor CB839 had decreased *Il-1*β expression (Fig. 2B), an effect that could be rescued by adding exogenous glutamine (Fig. 2B). We sought to test the role of *S. aureus* in vitro and found that keratinocytes treated with *S. aureus* induced *Il-1*β mRNA expression (Fig. 2B). Notably, CB839 significantly inhibited *S. aureus*–induced *Il-1*β expression (Fig. 2B), suggesting that induction is mediated by glutamine metabolism. In contrast, other metabolites had no effect on keratinocyte IL-1β production. Keratinocytes treated with lactase dehydrogenase inhibitor (FX11) or glucose oxidation inhibitor (UK5099) did not have significantly decreased Il-1β levels compared to vehicle-treated controls (Fig. 2C). However,

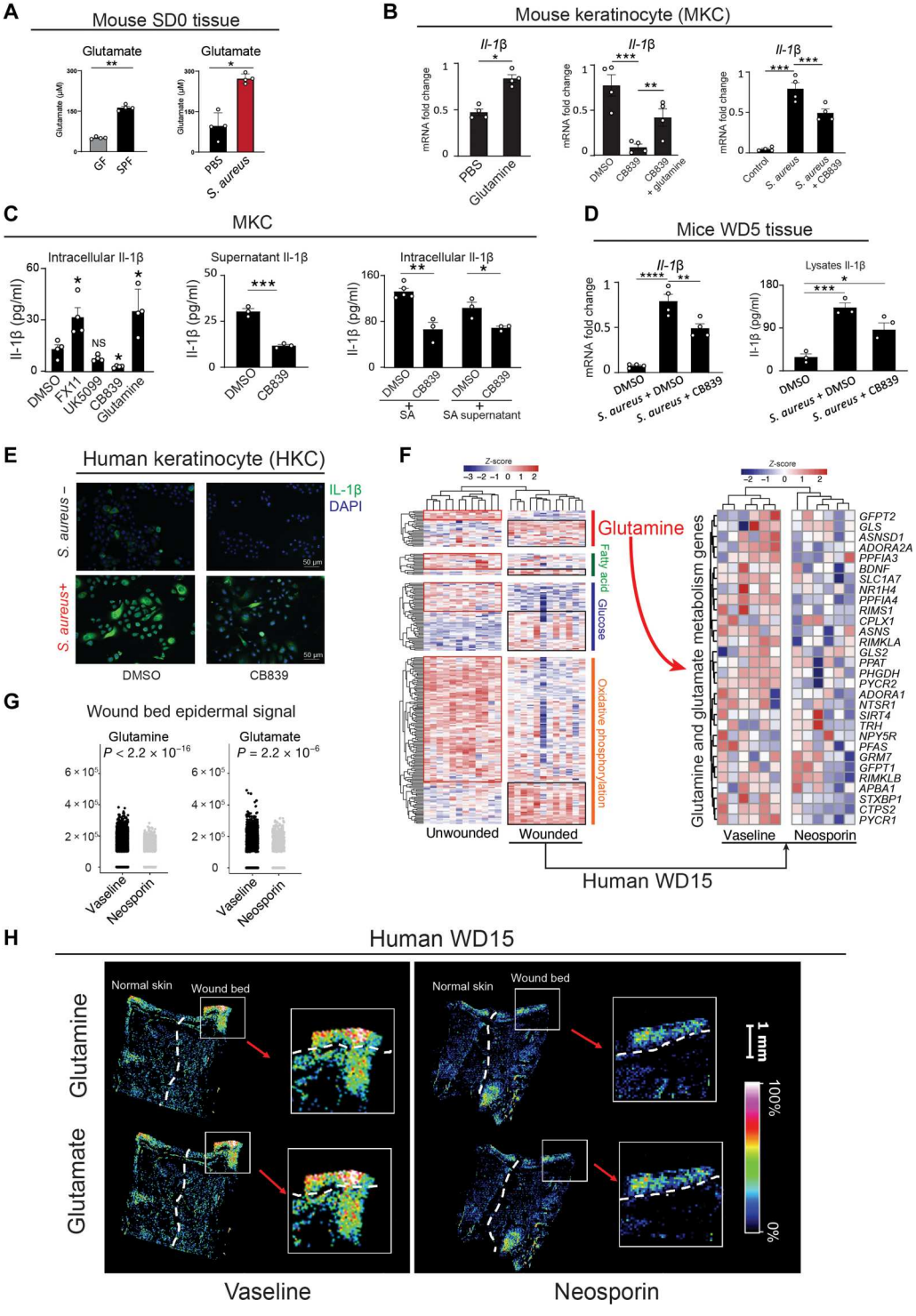

Fig. 2. Bacteria-induced keratinocyte IL-1β production via glutamine metabolism. (**A**) Detected by ELISA, glutamate expression of GF, SPF, PBS-treated, and *S. aureus*–treated mice at SD0. (**B**) *Il-1β* mRNA expression of mouse keratinocyte (MKC) treated with glutamine, CB839 (an inhibitor of glutamate production), or *S. aureus* as detected by qRT-PCR. DMSO, dimethyl sulfoxide. (**C**) As detected by ELISA, Il-1β expression of MKC treated with FX11, UK5099, CB839, glutamine, *S. aureus*, and *S. aureus* supernatant. (**D**) As detected by qRT-PCR and ELISA, Il-1β expression in mouse WD5 wound bed tissue treated with *S. aureus* and CB839. (**E**) IL-1β protein expression in human foreskin keratinocytes (HKC) treated with *S. aureus* and CB839 as detected by immunofluorescence (IF). DAPI, 4′,6-diamidino-2-phenylindole. (**F**) Metabolism gene signatures in microarrays of unwounded and WD15 human skin. (**G** and **H**) Glutamine and glutamate expression in Vaseline-treated and Neosporin-treated human WD15 wound bed tissues as detected by MSI (H) and quantification (G) as in Fig. 1, with same statistical and graphing methods. *n* = 3 to 6 independent animals or independent human samples per group.

CB839 inhibited mouse keratinocyte Il-1β protein expression and release (Fig. 2C). CB839 also inhibited the production of Il-1β protein induced by *S. aureus* and *S. aureus* supernatants, confirming the mRNA results (Fig. 2C). Last, we investigated that the in vivo effect of glutamine metabolism on the production of IL-1β. *S. aureus* induced and CB839 inhibited both Il-1β protein and mRNA production (Fig. 2D). In human keratinocytes, CB839 also inhibited IL-1β production (Fig. 2E). These results show that skin bacteria, specifically *S. aureus*, promote keratinocyte glutamine metabolism and that glutamine metabolism is essential for the production of keratinocyte IL-1β.

Last, we tested the effect of bacteria on human wound metabolism in a small trial of healthy adult volunteers by performing bilateral punch biopsy wounds of the skin at the popliteal fossae (behind the knees) and subsequent treatment with a vehicle (Vaseline petroleum jelly) or a topical antibiotic (Neosporin). A second biopsy was performed to collect healing tissue. In an analysis of the transcriptome, we found that wounding of skin induces large shifts in metabolic patterns and that glutamine metabolism was highly induced in wounded skin (Fig. 2F). This finding is consistent with previous studies showing that glutamine metabolism increases during damage response (*31*, *32*). Our previous research also showed that using antibiotic ointment significantly reduced wound healing speed and altered the microbiome in both mice and humans (*1*, *33*). Glutamine metabolism, glutamate metabolism, and bacterial relative abundance did not differ between the left and right sides on human unwounded skin (fig. S5, C and D). However, after wounding, the total amount of bacteria on the side treated with Neosporin was significantly lower than that on the side treated with Vaseline (fig. S5D). The Vaseline-treated side was characterized by a significant increase in the dominant bacteria, *Staphylococcus*, in the popliteal fossa (fig. S5E). In both unwounded and wounded skin, *S. aureus* and *Staphylococcus epidermidis* were the dominant *Staphylococcus* species (fig. S5F). Consistent with these results, antibiotic treatment significantly reduced glutamine metabolism genes in the human wound bed (Fig. 2F). Furthermore, MSI showed that glutamine and glutamate levels decreased in the antibiotic-treated human wound bed (Fig. 2, G and H, and fig. S4B). These data indicate that commensal bacteria on human skin can also induce glutamine metabolism and improve regeneration, which is consistent with our in vitro results (*1*).

Glutamine metabolism induces the expression of stem cell markers and regenerative signaling in vitro

We investigated the effect of glutamine metabolism on keratinocyte regeneration signals in vitro (*1*, *26*, *34*). We found that CB839 inhibited the regeneration signals *Wnt7b* and *Shh* and the stem cell marker *Krt15* and induced the terminal differentiation marker *Krt1* in keratinocytes (Fig. 3A). However, CB839 did not inhibit *Wnt7b* and *Krt15* in keratinocytes from *Myd88*$^{-/-}$ and *Il-1*β$^{-/-}$ mice (Fig. 3B). Thus, glutamine induces regeneration-associated genes through IL-1β–MyD88 signaling. CB839 inhibits the protein expression of active β-catenin and KRT15 in human keratinocytes but induces the protein expression of KRT1 (Fig. 3C). Notably, the addition of mouse recombinant Il-1β (rmIl-1β) can rescue the inhibition of *Wnt7b* and *Shh* and the promotion of *Krt1* by CB839 in mouse keratinocytes (Fig. 3D). These data suggest that IL-1β is a downstream signal of glutamine-induced regenerative gene expression.

Glutamate is required for baseline and bacteria-induced WIHN

We studied the effect of glutamine metabolism on hair follicle regeneration in vivo. The addition of exogenous glutamine to healing wounds induced WIHN (fold change = 2.2, $P = 2.8 \times 10^{-4}$), whereas CB839 inhibited WIHN (fold change = −3.2, $P = 5.4 \times 10^{-4}$) (Fig. 4A). Consistent with this effect, glutamine induced glutamate production at SD0, whereas CB839 inhibited it (Fig. 4B). To determine whether other metabolic pathways could affect WIHN, separate cellular respiration pathways were blocked (fig. S5G). Because previous studies have shown that lactate metabolism is essential for activating HFSCs, we used FX11 to inhibit lactase dehydrogenase (*24*). Although FX11 inhibited baseline WIHN (fold change = −2.3, $P = 1.2 \times 10^{-4}$), it did not inhibit *S. aureus*–induced WIHN ($P = 0.30$) (Fig. 4C). Hence, lactate metabolism promotes hair follicle regeneration but does not play a key role in the regeneration induced by bacteria. To confirm that the effect of CB839 on WIHN is not simply a result of metabolic deficiencies, we also reduced citric acid cycle metabolism by preventing pyruvate entry with the inhibitor UK5099 (fig. S5G). However, UK5099 did not inhibit hair follicle regeneration ($P = 0.31$) (Fig. 4D). In contrast, CB839 inhibited *S. aureus*–induced WIHN (fold change = −2.3, $P = 4.9 \times 10^{-4}$; Fig. 4E). It also inhibited baseline and *S. aureus*–induced glutamate and Il-1β expression at SD0 (Fig. 4F). This finding is consistent with our in vitro data, which showed that glutamate expression decreases when mouse keratinocytes are cultured in glutamine-deficient medium (fig. S5H). Similarly, in the absence of glutamine, bacterially induced glutamate expression in keratinocytes also decreased (fig. S5H). Collectively, these results indicate that hair follicle regeneration induced by bacteria depends on glutamine metabolism. Last, to confirm that the promotion of WIHN by glutamine metabolism is keratinocyte dependent, we used keratinocyte Myd88 and myeloid Myd88 knockout mice to exclude the role of myeloid Myd88. We treated WT, *Il-1*β$^{-/-}$, *K14-Myd88*$^{-/-}$, and *LysM-Myd88*$^{-/-}$ mice with glutamine. Glutamine induced WIHN only in WT and *LysM-Myd*88$^{-/-}$ mice (fold change = 2.5, $P = 3.4 \times 10^{-4}$), indicating that glutamine metabolism promotes hair follicle regeneration through IL-1β–keratinocyte–dependent Myd88 signaling in keratinocytes (Fig. 4G).

S. aureus stimulates glutamine metabolism, IL-1β production, and WIHN through hypoxia-induced HIF-1α signaling

Previous studies have shown that increased bacterial loads, especially of *S. aureus*, can induce hypoxia in the skin. Separately, studies have shown that hypoxia-induced HIF-1α signaling promotes glutamine metabolism and IL-1β synthesis (*19*, *35*, *36*). We sought to determine the mechanism by which bacteria promote glutamine metabolism to induce IL-1β production using GSEA to detect the state of hypoxia in human and mouse wounds under different bacterial loads. We reexamined the three human and mouse studies correlating bacterial load to regeneration and a fourth comparison of high versus low WIHN among different mouse strains. In all cases, regenerative capacity was correlated with a hypoxic transcriptomic signature (Fig. 5A). Most hypoxia-related genes are highly expressed in wounds with high regeneration. *Hif-1*α mRNA was especially high, as confirmed by quantitative polymerase chain reaction (PCR) (Fig. 5, B and C). We examined the changes in keratinocyte glutamine metabolism and *Il-1*β under hypoxic conditions

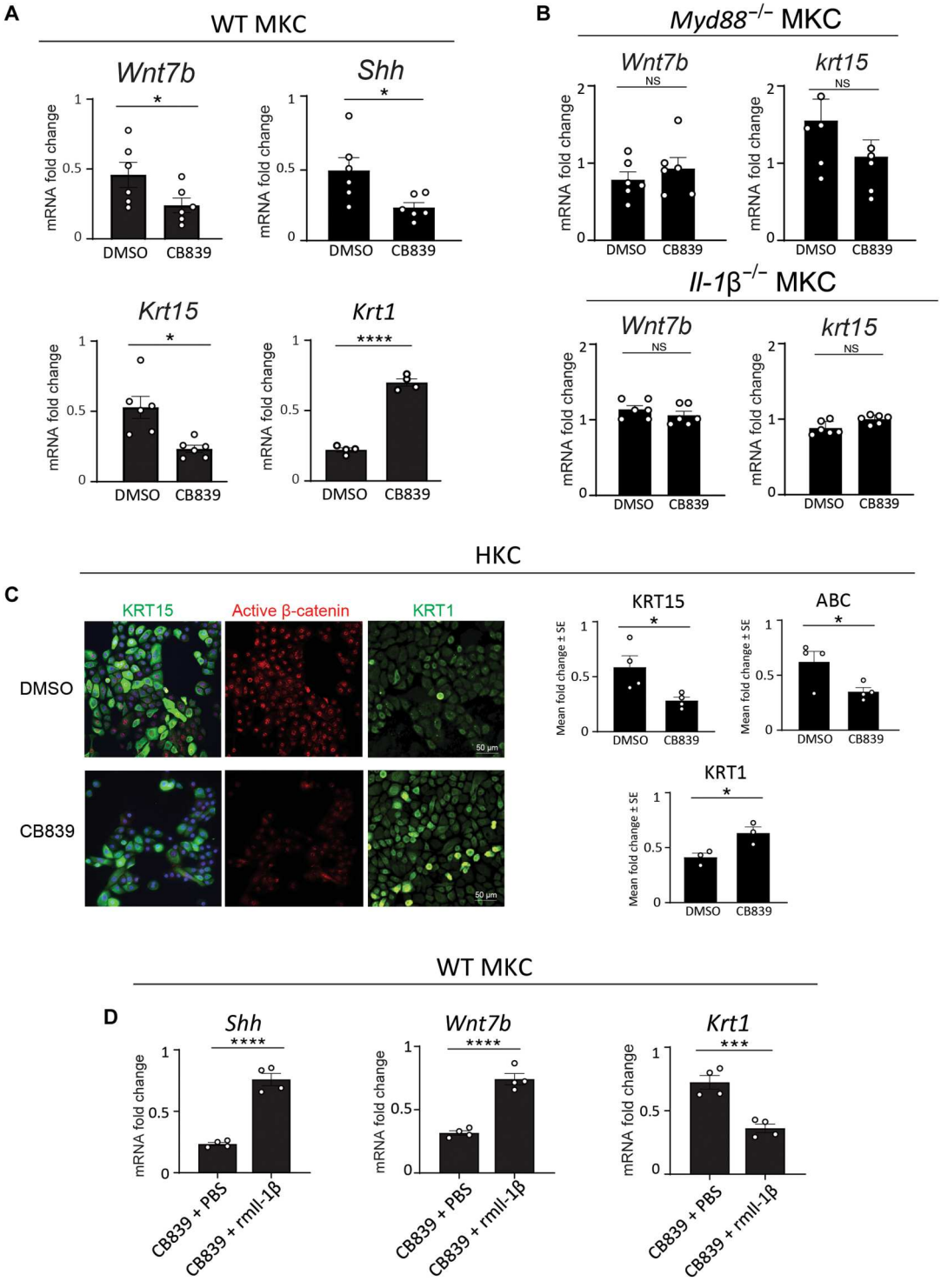

Fig. 3. Glutamine metabolism induces the expression of stem cell markers and regenerative signaling in vitro. (**A**) The mRNA expression by qRT-PCR of regeneration markers *Wnt7b*, *Shh*, and stem cell marker *Krt15* and differentiation marker *Krt1* in CB839 treated mouse keratinocytes (MKC). (**B**) *Wnt7b* and *Krt15* mRNA expression in CB839 treated *Myd88*$^{-/-}$ and *IL-1*$\beta^{-/-}$ MKC. (**C**) Immunofluorescence (left) and quantification (right) of CB839-treated human keratinocyte (HKC) stained for KRT15, active β-catenin (ABC), and KRT1 expression. (**D**) The mRNA expression of *Shh*, *Wnt7b*, and *Krt1* of CB839 and mouse rmIL-1β–treated MKC. Statistics and graphing as in Fig. 1. *n* = 3 to 6 independent animals or independent human samples per group.

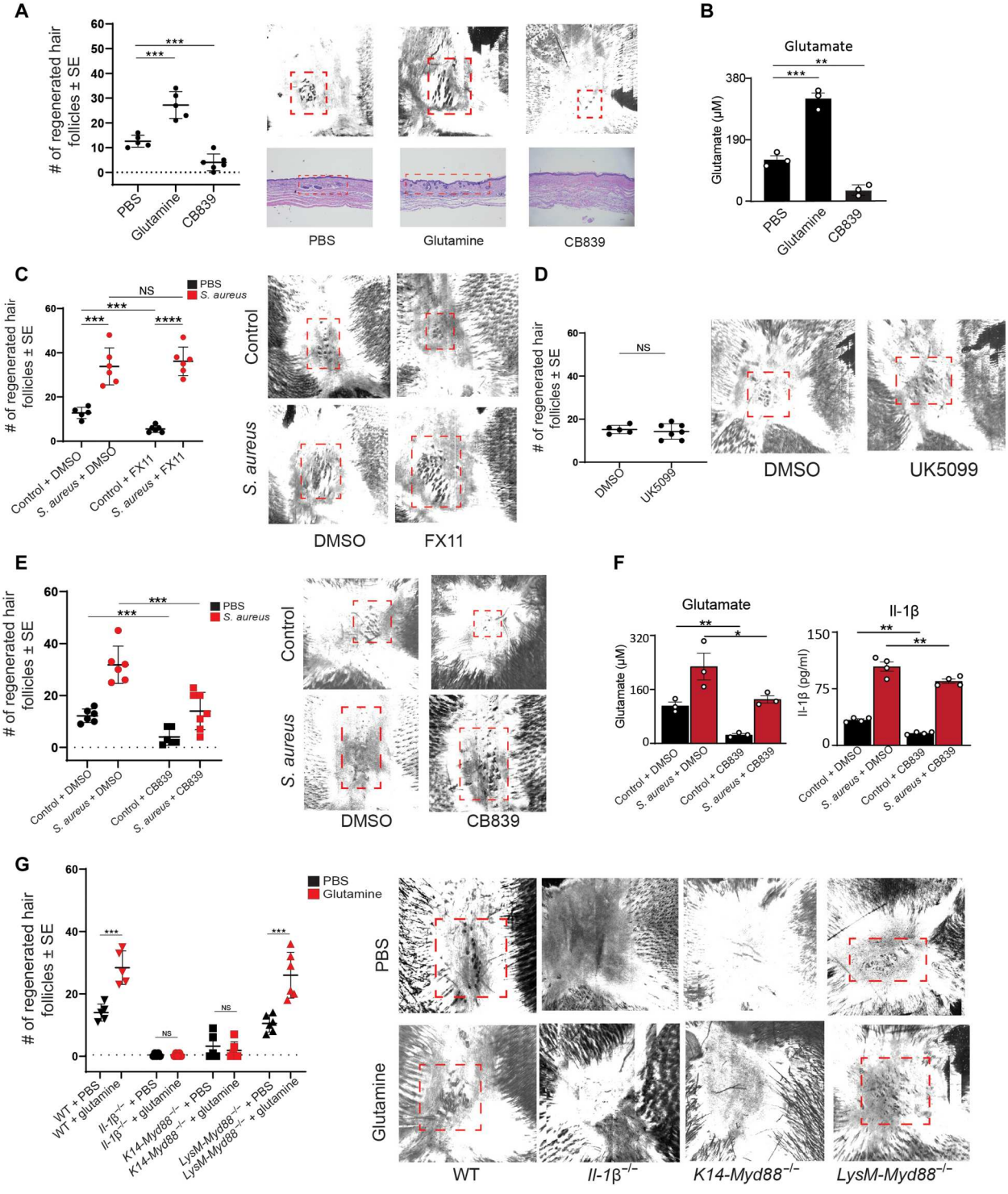

Fig. 4. Glutamate is required for baseline and bacteria-induced WIHN. (**A**) WIHN of glutamine and CB839 treated (WD3) mice, compared to PBS controls, as detected by confocal scanning laser microscopy (CLSM) (top right), hematoxylin and eosin (H&E) staining (bottom right), and quantification (left). The red dashed squares indicate the regenerative hair follicles. (**B**) Glutamate production in SD0 mouse wound beds as measured by ELISA. (**C**) WIHN of *S. aureus*– and FX11-treated (WD3) mice, as detected by CSLM (right) and quantification (left). (**D**) WIHN of UK5099-treated (WD3) mice, as detected by CSLM (right) and quantification (left). (**E**) WIHN of *S. aureus*– and CB839-treated mice, as detected by CSLM (right) and quantification (left). (**F**) Glutamate and Il-1β production in *S. aureus*– and CB839-treated mice SD0 wound beds as measured by ELISA. (**G**) WIHN of glutamine-treated or untreated WT, *Il-1β*$^{-/-}$, *K14-Myd88*$^{-/-}$, and *LysM-Myd88*$^{-/-}$ mice (right) with quantification (left). Statistics and graphing as in Fig. 1. $n = 3$ to 7 independent animals per group.

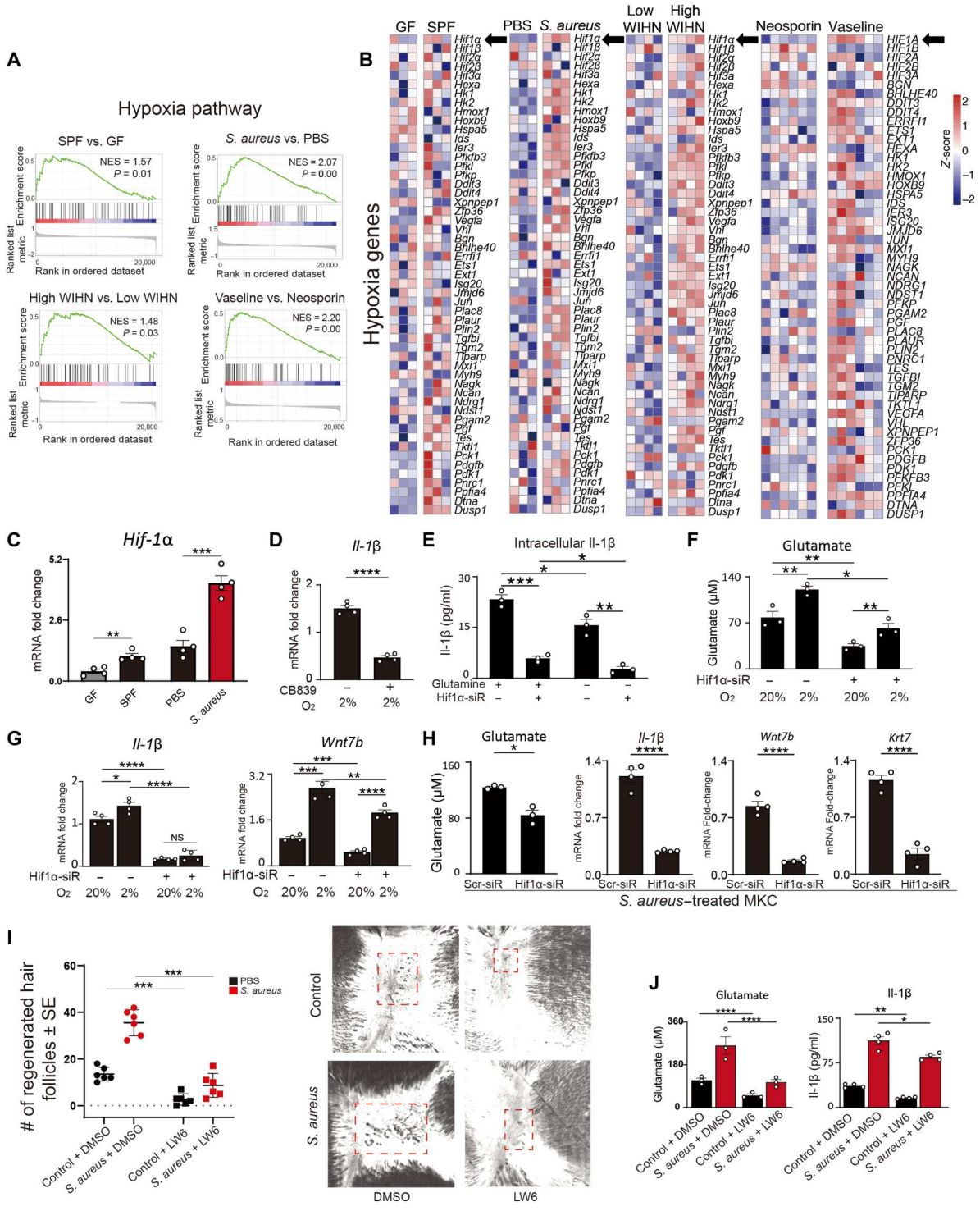

Fig. 5. Bacteria-stimulated glutamine metabolism and IL-1β production through hypoxia-induced HIF signaling. (**A** and **B**) GSEA of DEGs (A) and relative mRNA (B) of hypoxia genes detected by microarray in SD0 wound bed of GF, SPF, PBS-treated, *S. aureus*–treated, low WIHN strain (C57BL/6), and high WIHN strain (B6/FVB/SJL) mice as well as in Vaseline- and Neosporin-treated human wound bed. (**C**) qRT-PCR–determined mRNA expression of *Hif-1*α in SD0 skin of GF, SPF, PBS-treated, and *S. aureus*–treated mice. (**D**) *Il-1*β mRNA expression by qRT-PCR under hypoxic conditionsin MKC. (**E**) Il-1β expression in MKC treated with or without glutamine and *Hif-1*α siRNA, as detected by ELISA. (**F**) Glutamate expression of MKC treated with or without *Hif-1*α siRNA under hypoxic or normoxic conditions, as detected by ELISA. (**G**) *Il-1*β and *Wnt7b* expression of MKC treated with or without *Hif-1*α siRNA under hypoxic or normoxic conditions, as detected by qRT-PCR. (**H**) Glutamate, *Il-1*β, *Wnt7B*, and *Krt7* expression of *S. aureus*–induced MKC treated with or without *Hif-1*α siRNA, as detected by ELISA and qRT-PCR. Scr-siR indicates scramble siRNA. (**I**) WIHN of *S. aureus* and LW6 treated mice, as detected by CSLM (right) and quantification (left). The red dashed square indicate the regenerative hair follicles. (**J**) Glutamate and Il-1β expression of *S. aureus*– and LW6-treated (WD3) mice SD0 wound bed, as detected by ELISA. Graphing and statistics as in Fig. 1. *n* = 3 to 6 independent animals per group.

in vitro. CB839 inhibited the expression of *Il-1*β under 2% oxygen (Fig. 5D), as it had under normal oxygen conditions (Fig. 2B).

Subsequently, we compared the effects of Hif-1α on glutamine metabolism and Il-1β expression in cultured mouse keratinocytes in vitro under normal oxygen (20%) and hypoxic conditions (2% oxygen). Under normoxia, knockdown of *Hif-1*α with *Hif-1*α small interfering RNA (siRNA) (fig. S5I) reduced Il-1β production, but addition of exogenous glutamine partially reversed this effect, suggesting that glutamate mediates Hif-1α induction of Il-1β production (Fig. 5E). We found that the hypoxic environment induced keratinocyte glutamine metabolism, *Il-1*β expression, and expression of proregenerative *Wnt7b* when compared to levels in normoxic cells (Fig. 5, F and G). By knocking down *Hif-1*α, we inhibited *Il-1*β expression of keratinocytes cultured under hypoxic conditions (Fig. 5G). These results show that hypoxia induces glutamine metabolism through HIF-1α signaling, which then induces IL-1β production and regeneration signals (Fig. 5, E to G). Our bioinformatic analyses revealed that SLC1A7, a glutamate transporter, is highly expressed in mouse and human skin with high bacterial loads and high WIHN (Figs. 1B and 2F). A previous study showed that glutamate transporter expression is mediated by HIF-1α signaling (*37*). Therefore, we knocked down the expression of Slc1a7 in the keratinocytes. Although knocking down Slc1a7 reduced glutamate expression in keratinocytes, glutamate expression induced by *S. aureus* did not decrease significantly (fig. S5J). Thus, other glutamine transporters might play a compensatory role when glutamate expression is stimulated by *S. aureus*. Furthermore, silencing of *Hif-1α* also significantly reduced *S. aureus*–induced glutamine metabolism and the expression of *Il-1*β, regeneration signal *Wnt7b*, and stem cell marker *Krt7* (Fig. 5H).

In vivo, we confirmed our findings by injecting the HIF-1α inhibitor LW6 into mouse wounds and evaluating WIHN. We observed that LW6 inhibited both baseline WIHN (fold change = −5.1, $P = 2.0 \times 10^{-5}$) and *S. aureus*–induced WIHN (fold change = −4.1, $P = 2.8 \times 10^{-6}$) (Fig. 5I). Likewise, LW6 inhibited the expression of glutamate and Il-1β in the wound at the beginning of hair follicle regeneration (Fig. 5J). These results indicate that hypoxia-induced HIF-1α signal stimulates glutamine metabolism and IL-1β production in keratinocytes in vitro and in vivo, inducing proregenerative signals and thereby promoting WIHN.

Hypoxia and glutamine metabolism in keratinocytes during WIHN

We found that bacteria promote keratinocyte hypoxia and glutamine metabolism in vivo and in vitro, which, in turn, induce regeneration in mice and humans. We verified our finding in public single-cell RNA sequencing (scRNA-seq) databases for four conditions: normal skin, small wound, large wound center (WIHN), and large wound periphery (non-WIHN) under GSE108677 (*38*). Five cell types have been defined according to known markers, including keratinocytes, fibroblasts, immune cells, endothelial cells, and peripheral cells (fig. S6A) (*39*). Previous studies have shown that γδT cells in the wound bed release Fgf9 to activate the Wnt signal of dermal fibroblast, which is necessary to initiate hair follicle regeneration. Afterward, during reepithelialization (SD0), epidermal keratinocytes coalesce to the hair germ (HG) and release Wnt ligands to activate dermal papilla (*40*, *41*). These extracellular signals promote embryonic-like hair follicle morphogenesis. Given such examples of the importance of communications between immune cells, fibroblasts, and keratinocytes in WIHN, we investigated the different interactions between keratinocytes and other cells in the microenvironment of WIHN (wound center) and non-WIHN (wound periphery). We found that the intensity of intercellular communication in WIHN was greater than that of non-WIHN, especially for intercellular growth factors (fig. S6B).

We focused on keratinocytes for in-depth exploration (fig. S6A, black arrow). Consistent with the results of our bulk RNA-seq on mice and humans, scores for hypoxia, oxidative phosphorylation, and glutamine and glutamate metabolism were significantly higher in keratinocytes isolated from wounds than in those isolated from normal skin. These scores were also higher in the large wound centers (WIHN) than in the periphery (non-WIHN), showing that keratinocytes in the wound bed, especially in the regenerative hair follicles, required increased energy and glutamine metabolism (fig. S6C). We found that in keratinocytes, the hypoxia score was positively correlated with IL-1 signal ($R = 0.69$, $P < 2.2 \times 10^{-16}$) scores (fig. S6D). By comparing the central (WIHN) and peripheral (non-WIHN) keratinocytes, we found that the WIHN keratinocytes highly expressed protein synthesis and mitochondrial metabolism pathways, which induced HG development. In contrast, the non-WIHN keratinocytes highly expressed the extracellular matrix synthesis pathway, which is known to be elevated in scar formation (fig. S6E). Because WIHN is a dynamic process, we used pseudotime analysis to reconstruct the development of keratinocytes (fig. S6F). We found that in large wounds, especially at the center (WIHN), keratinocytes were concentrated in the early developmental stage, when the stem cell potential was stronger, whereas in small wounds (non-WIHN), keratinocytes were concentrated in the late developmental stage, when the stem cell potential was weaker (fig. S6, F and G). Through the clustering of developmental reconstruction genes, we found that cells in the early stages of development highly expressed p53, cell cycle, glutathione metabolism, and Hif-1 signals (fig. S6H). In addition, stem cell and developmental markers (fig. S6I) and hypoxia-related genes (fig. S6J) decreased with pseudotime. These data are consistent with previous studies, which showed that hypoxia is critical to the metabolic milieu of stem cell niches (*42*).

Hypoxia and glutamine metabolism during hair follicle development in WIHN

To further investigate the changes in energy metabolism of keratinocytes during hair follicle regeneration at the single-cell resolution and to confirm the effects of hypoxia and glutamine metabolism on keratinocyte differentiation and HG development, we performed scRNA-seq. We compared the wound center (WIHN) and wound periphery (non-WIHN) in additional mice (five mice per group). Previous studies have shown that gene transcription is altered before keratinocytes migrate to the center of the wound, suggesting that the fate of keratinocytes is determined before HG development (*41*, *43*). We collected the wound bed tissue immediately before hair follicle regeneration (SD0) for sequencing. We clustered the cells in the wound center and periphery separately and used multiple markers to define different cell clusters (Fig. 6, A and B, and fig. S7, A to D). Five cell types were defined: keratinocytes, fibroblasts, immune cells, endothelial cells, and peripheral cells (Fig. 6, A and B). We found more interactions between different cell types in the wound center than in the periphery, especially communication between various cells and keratinocytes (Fig. 6C and fig. S7E).

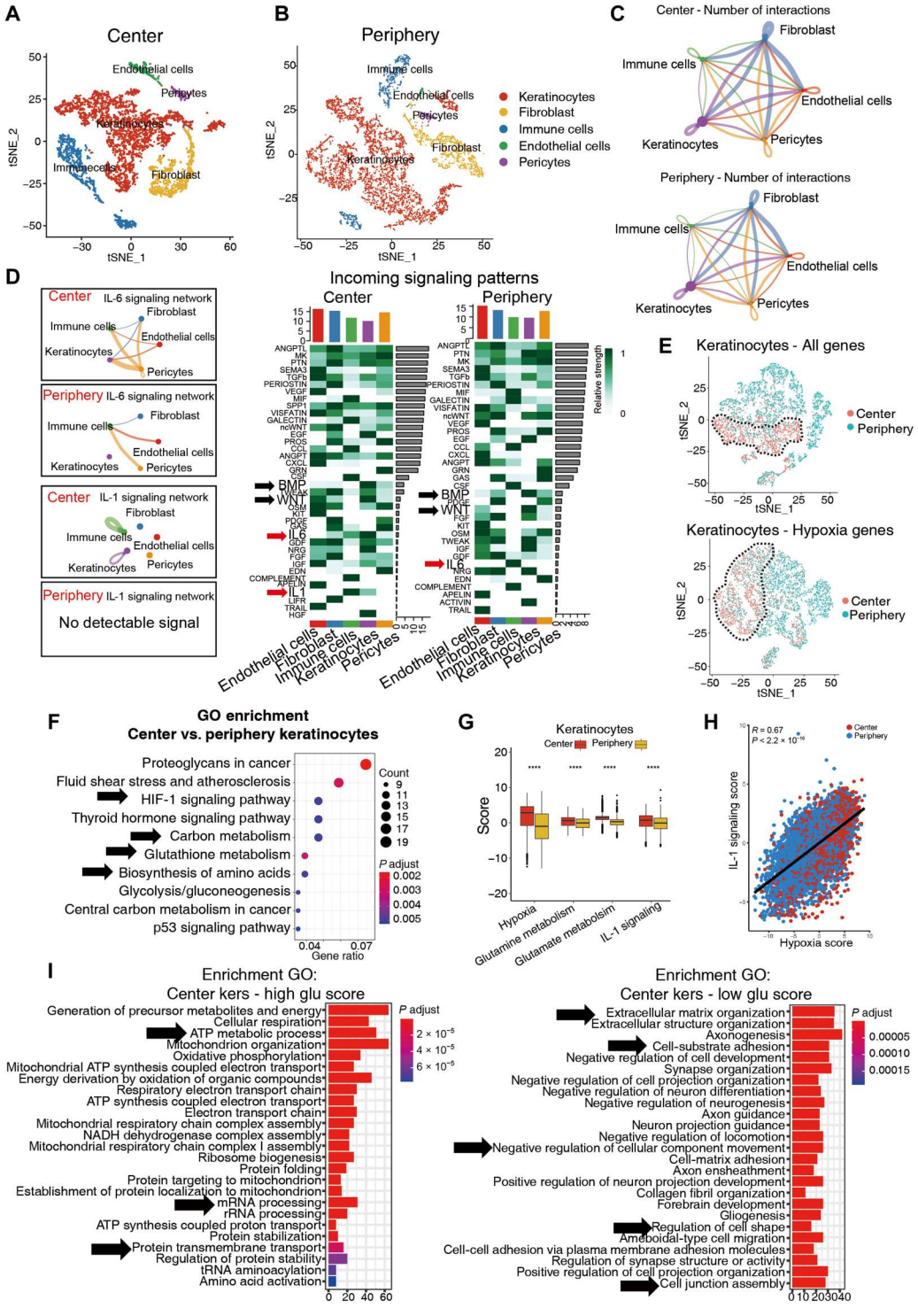

Fig. 6. Hypoxia and glutamine metabolism are elevated in wound center versus periphery in WIHN. (**A** and **B**) t-SNE plots visualization of WT mice SD0 wound center (high-WIHN, A) and SD0 wound periphery (non-WIHN, B) by scRNA-seq. Five mice were pooled per sample. (**C**) The overall number of cellular interactions in the wound center (top) or the periphery (bottom) at SD0 as detected by CellChat algorithm. Thicker lines indicate more interactions. (**D**) Specific cell-cell interaction patterns of IL-6 and IL-1 (left). Specific incoming signals of each cell type in the wound center and periphery at SD0 (right). Outgoing signals are shown in fig. S7F. (**E**) The t-SNE plots clustered by all gene expression profiles (top) or just by hypoxia gene expression profiles (bottom) of SD0 keratinocytes. (**F**) GO enrichment analysis of keratinocytes in the wound center versus the periphery. (**G**) Scores for hypoxia, glutamine, and glutamate metabolism and IL-1 signaling calculated by PCA method in keratinocytes comparing wound center versus wound periphery. (**H**) The correlation of IL-1 signaling score and hypoxia score in keratinocytes as analyzed by Spearman correlation. The scores of center and periphery of the wound are shown in red and blue, respectively. (**I**) GO enrichment analysis in the wound center keratinocytes with a high glutamate score (left) compared to those with a low glutamate score (right). The high and low glutamate scores were calculated using the PCA method as detailed in Materials and Methods. Box plot graphs indicated the value of minimum, first, quartile, median, third quartile, and maximum. Unless otherwise noted, statistics as in Fig. 1. NADH, reduced form of nicotinamide adenine dinucleotide.

To explore the specific signals that play a role in the communication between cells, we listed the signals that originated or affected various cells (Fig. 6D and fig. S7, F and G). The bone morphogenic protein (BMP) signal that acts on fibroblasts and pericytes was substantially weaker in the center of the wound than in the periphery, whereas the Wnt signal that acts on vascular endothelial cells and fibroblasts was substantially stronger in the center of the wound and weaker in the periphery. These findings support studies showing that Wnt induces hair regeneration, and BMP inhibits it (*41*, *44*). The overall IL-6 signal acting on keratinocytes was substantially stronger in the center of the wound than at the periphery (Fig. 6D, red arrow). In addition, more IL-6 signaling from each cell type acted on keratinocytes in the wound center, consistent with our previous study (Fig. 6D, left) (*26*). We also noticed that

the IL-1 signal was absent from the wound periphery and was expressed only in the center of the wound. The specific expression pattern showed that keratinocytes release IL-1, which acts in an autocrine fashion, supporting the results described above (Fig. 6D) (*1*).

After establishing the interactions between different types of wound cells, we focused on the interactions between keratinocytes. When we used all genes for unsupervised clustering, the keratinocytes in the wound center clustered apart from those in the periphery, indicating that they had different gene expression patterns (Fig. 6E, top). The same pattern was observed when we used only hypoxia-related gene sets for unsupervised clustering. Keratinocytes in the wound center still clustered together, as did those in the periphery, with little overlap between the two groups (Fig. 6E, bottom). This phenomenon did not occur with other gene sets (fig. S7H), suggesting that hypoxia gene expression signatures are a major differentiator of central versus peripheral keratinocytes. We assessed the metabolic status of the keratinocytes in the center and periphery. Enrichment analysis of differentially expressed genes (DEGs) between center and peripheral keratinocytes showed that the HIF-1 signal, carbon metabolism signal, glutathione metabolism, and amino acid biosynthesis were highly expressed in the center (Fig. 6F). We found that the keratinocytes in the center had higher hypoxia, glutamine metabolism, and IL-1 signal scores (Fig. 6G). Thus, the keratinocytes in the high-WIHN wound center appear to have a higher hypoxic status and glutamine metabolism. We used proteomics to confirm these findings. Consistent with the scRNA-seq data and our previous study, retinoic acid metabolism, glutamate metabolism, and glutathione were higher in the wound center, whereas fatty acid metabolism and glucose metabolism were lower (fig. S7I) (*34*). The glutamine metabolism, hypoxia, and IL-1 signaling scores calculated from the proteomic data were higher in the wound center, whereas the keratinocyte differentiation score was lower (fig. S7J). We also found that the hypoxia score was positively correlated with the IL-1 signaling score ($R = 0.67$, $P < 2.2 \times 10^{-16}$) (Fig. 6H). These results verified the high glutamine metabolism, hypoxia, and IL-1 signaling in the high WIHN area at both the transcript and protein levels.

Because keratinocytes in the wound center are the source of epithelial components for regenerating hair follicles, we isolated them for analysis. We carried out a GO enrichment analysis on the DEGs associated with high and low glutamine metabolism and found that keratinocytes with high glutamine metabolism have stronger adenosine 5′-triphosphate synthesis, mRNA, and protein synthesis pathways, which are necessary for hair follicle development (Fig. 6I). Keratinocytes with low glutamine metabolism had stronger extracellular matrix formation, intercellular adhesion, and cellular junctions, which are necessary for the formation of scar tissue and likely inhibit WIHN (Fig. 6I).

To explore the fate of different keratinocyte subtypes, we clustered the keratinocytes in the wound center and labeled them according to known markers to identify six subtypes: basal1, basal2, basal3, proliferative, spinous, and HG (Fig. 7, A and B) (*39*, *45*). Specifically, we used markers such as *Krt17*, *Lef1*, *Krt79*, and *Sox9* to mark HG keratinocytes and *Col17a1*, *Cox-2*, and *Ube2c* to mark basal and proliferating keratinocytes (Fig. 7, A to D). Compared with other cell types in the wound center, keratinocytes had stronger IL-1 and IL-6 signal inputs as well as stronger IL-1 signal output (fig. S7K). Moreover, HG keratinocytes had significantly higher hypoxia, glutamine, and glutamate metabolisms and IL-1 signaling than other keratinocytes, which is consistent with previous studies (Fig. 7E) (*1*, *14*).

Because WIHN is a dynamic process, to clarify the different states of basal cells in the context of epidermal differentiation, we calculated the differentiation state of keratinocytes using pseudotime analysis. The development pattern followed the direction of basal, spinous, proliferative, and HG keratinocytes (Fig. 7, F and G). The signature genes changed from stem cell markers to mature markers as pseudotime progressed (Fig. 7H). The expression of HG markers gradually increased (Fig. 7, H and I). We divided the developmental stages of HG into six incremental stages: A to F (Fig. 7J). As HG cells developed, the metabolism of hypoxia and glutamate showed an overall upward trend (Fig. 7K). The IL-1 signal also somewhat increased; however, glucose metabolism did not change significantly (Fig. 7K). These results suggest that increased hypoxia and glutamine metabolism can maintain the stemness of keratinocytes and promote hair follicle development (fig. S7L).

DISCUSSION

The microbiome contributes to host health through a number of means, including influencing metabolism (*6*). However, despite important but disparate work in this area, how metabolism explains the microbiome's proregenerative effects has not been connected into a coherent unified physiologic mechanism in mice and humans. In our previous study, we verified that high bacterial load can promote hair follicle regeneration in six groups of mice with increasing bacterial loads. Although *S. aureus* has the strongest ability to induce hair follicle regeneration, *Staphylococcus*, *Pseudomonas*, and *Streptococcus*, the top three resident bacteria in mouse skin, can all induce hair follicle regeneration. Also, knockout of TLR2 and TLR3 does not affect the promotion of hair follicles regeneration by bacteria (*1*). These results using pleiotropic bacteria that can all induce regeneration independently of specific TLR sensors suggests that skin-resident bacteria promote hair follicle regeneration not through specific bacterial biology but through nonspecific, generalized pathways. Consistent with this model, we propose a mechanism whereby *S. aureus* nonspecifically induces hair follicle regeneration by local hypoxia and ensuing glutamine production. These findings add an unappreciated angle to the importance of glutamine metabolism in regeneration (*35*). In the skin regeneration model, we find that the skin commensal microbiome induces hypoxia in the wound microenvironment and activates HIF1α signaling, promotes glutamine metabolism in keratinocytes, and thus activates downstream IL-1β signaling to promote WIHN. Although the WIHN phenomenon does not exist in human skin, commensal microbes promote both mouse and human wound healing speed, illustrating an overlapping mechanism (*1*). These results highlight the importance of the environment on hair follicle regeneration and wound healing.

Glutamine metabolism can promote regeneration by increasing the efficiency of energy metabolism to activate stem cells and by increasing the antioxidant effect of reduced glutathione to increase the survival rate of stem cells (*32*, *35*). However, the mechanism of how glutamine affects regeneration is still unclear; for example, the relationship between glutamine and immune stimulation is ambiguous (*16*, *18*, *46*). Our work shows that glutamine promotes

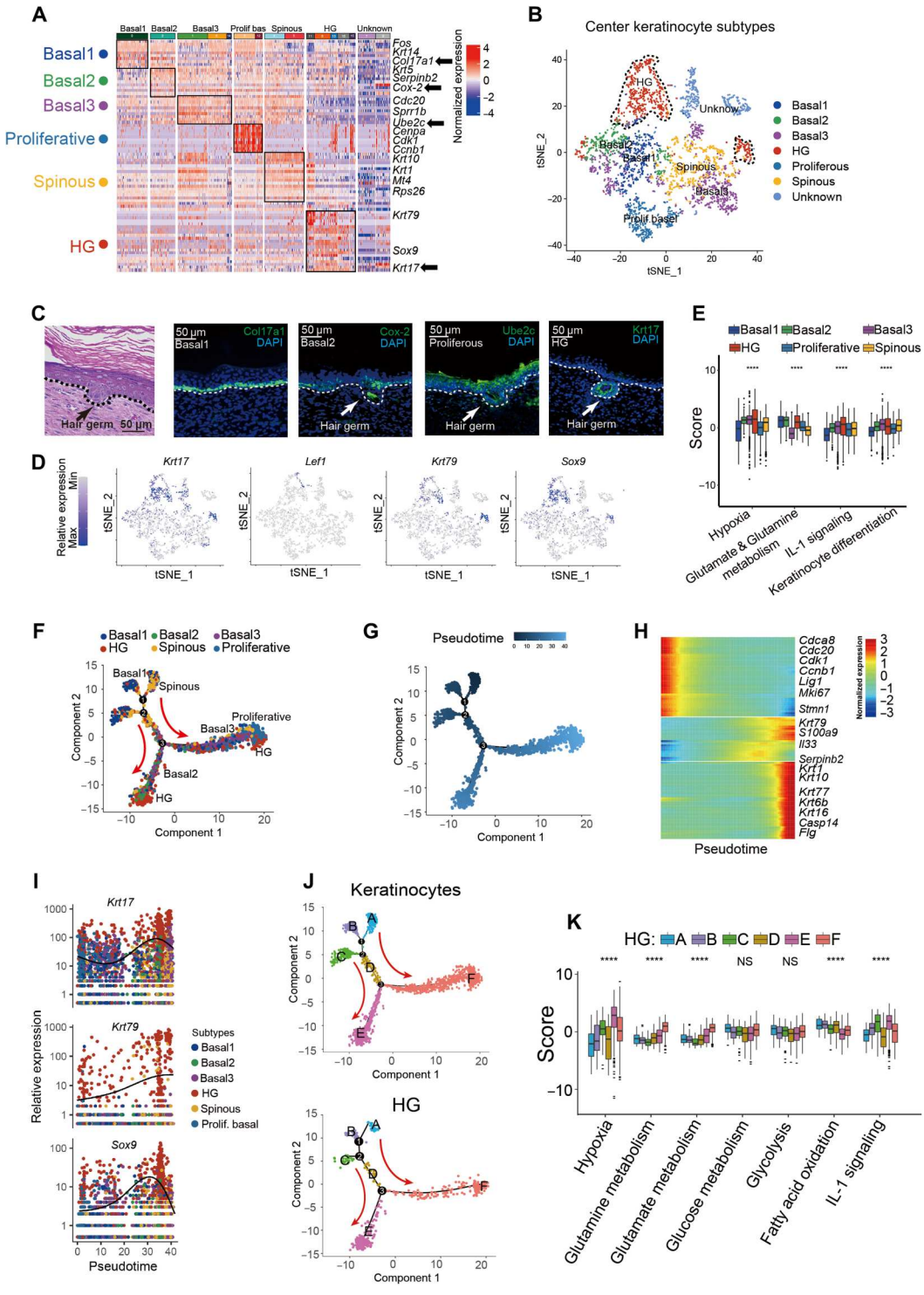

Fig. 7. Hypoxia and glutamine metabolism correlate to hair follicle development in WIHN. (**A**) Heatmap for canonical keratinocyte marker genes in each cluster of the wound center from scRNA-seq of SD0 samples. (**B**) The t-SNE plot shows clustering of SD0 wound center keratinocytes subpopulations. (**C**) H&E, Col17a1, Cox-2, Ube2c, and Krt17 staining of SD0 wounds to establish location of basal1, basal2, proliferous, and HG keratinocytes. Scale bars, 50 μm. (**D**) Expression of HG marker genes to identify the HG cluster in t-SNE plots. (**E**) The scores for hypoxia, glutamine, and glutamate metabolism and IL-1 signaling in keratinocytes subpopulations. (**F** and **G**) Pseudotime analysis plotting the development pattern of basal, spinous, proliferative, and HG keratinocytes. (**H**) The heatmap of differentiation markers with pseudotime. (**I**) Pseudotime plot depicting the abundance of HG markers *Krt17*, *Krt79*, and *Sox9* as divided by keratinocyte subpopulation. (**J**) Pseudotime analysis divided all keratinocytes (top) and HG (bottom) into six stages according to the developmental sequence; the different stages are indicated by different colors labeled A to F. (**K**) The gene expression scores for hypoxia, glutamine, and glutamate metabolism, and IL-1 signaling pathways as divided by HG developmental stage. Box plot graphs indicated the value of minimum, first, quartile, median, third quartile, and maximum. Statistics as in Fig. 1.

regeneration by inducing the production of IL-1β in keratinocytes, consistent with reports that serine and succinate promote the production of IL-1β, both in a glutamine-dependent manner (*12*, *13*). In other contexts, IL-1β production is also increased through the activation of glutamate receptors, for example, in the nervous system (*47*, *48*). In contrast, reducing glutamine in the brain and airways reduces the production and release of IL-1β and cellular inflammation (*49*, *50*). Others have shown that the exogenous addition of glutamine increases IL-1β and that exogenous IL-1β induces glutamine metabolism (*18*, *46*). However, multiple reports instead show that glutamine inhibits immune responses (*16*, *17*). Our research places glutamine in a more proinflammatory role and shows that inhibiting glutamine metabolism in keratinocytes reduces the expression of IL-1β. We found that inhibition of the

glutamine transporter SLC1A7 could inhibit keratinocytes baseline glutamate but not inhibit *S. aureus*–induced keratinocytes glutamate expression, suggesting that other glutamate transporters compensate for bacterial-induced glutamate transport in keratinocytes. Subsequent studies need to further explore the effect of bacteria on glutamate transporters. Nevertheless, our work now places the effects of glutamate on IL-1β into an important and underappreciated physiologic context of how the microbiome promotes regeneration. In conclusion, in both mice and humans, glutamine metabolism has a complex regulatory effect on inflammatory factors in the microenvironment, highlighting the importance of metabolic balance.

In fig. S5D, the wound bed treated with Vaseline has a high *Staphylococcal* variance, which we speculate is due to unique immune and colonization conditions in the wounds of different human volunteers. To control for the variation in *Staphylococcal* levels, the relative quantification of GLS expression to *Staphylococcus* abundance in six volunteers was performed by Spearman correlation analysis, and it was found that they were highly positively correlated ($R = 0.91$, $P = 0.011$). This suggests that, although there was variance in volunteers, the correlation still supports the notion that *Staphylococcus* promotes glutamine metabolism. In the future, larger clinical sample sizes where these absolute measurements are all made in the same patient will allow better study of the relationship between wound bed microbiota and metabolites.

Both our current findings and our previous studies have shown that IL-1β induces WIHN (*1*). However, a recent study showed that obesity accelerates hair depletion through IL-1R signaling (*51*), likely reflecting a difference in the response to IL-1β in the context of regeneration versus homeostatic maintenance. Similar to our findings, paralog IL-1α has been shown to activate HFSCs and up-regulate IL-36α and IL-6 to promote WIHN (*26*, *52*, *53*). Together, the evidence suggests that IL-1 signaling is a powerful proregenerative cue in response to skin damage.

Our work highlights important future work for the field. One important question is to definitively determine and verify the origin of different hypoxia levels among the models discussed (Fig. 5A). While SPF mice might have more hypoxia in wounds than GF mice because of colonizing bacteria, this should be verified experimentally. More intriguing is to explain why different strains of mice have different wound hypoxia levels that correspond to WIHN (fig. S1A). Similarly, whether some bacteria might induce or inhibit more hypoxia than others to enhance or inhibit regeneration and the generalizability of our experimental findings with *S. aureus* need further study. Another question to study is how the use of ointment during wounds might aid wound bed hypoxia. Also, although we found that hypoxia promotes regeneration by inducing glutamine metabolism in the wound bed, the relationship between hypoxia and other WIHN-promoting signals such as IL-6 and other metabolic pathways is still unknown. In the future, a more detailed mechanism by which hypoxia promotes skin regeneration needs to be explored. Last, future critical work will test whether any of these mechanisms might explain the lack of clear WIHN in humans.

Our findings that the skin microbiome promotes skin and hair follicle regeneration by activating glutamine metabolism in keratinocytes have important therapeutic implications. Indiscriminate use of topical antimicrobials should be reconsidered, as it may disrupt proregenerative signaling by resident flora. These agents are best reserved for situations of gross bacterial contamination or in patients with diabetes, immunosuppression, or known alterations in skin microbiota, such as those with chronic wounds. Second, the finding that glutamine induces skin regeneration in an IL-1β–dependent fashion suggests that simple addition of glutamate or IL-1β may promote wound healing, for example, in chronic wounds. Developing agents to manipulate these pathways is an important area for future investigation. In addition, while we observe beneficial roles for commensal *S. aureus* in our system, a fuller description of which bacteria can promote regenerative healing and how they interface with host factors awaits future studies in clinically relevant contexts. Such work will likely lead to improved, more precise therapies for millions of patients suffering from acute and chronic wounds.

MATERIALS AND METHODS

Animals

The backgrounds of all mice are based on C57BL/6J. The GF mice were provided and managed by the Germ-Free laboratory of the Johns Hopkins Bloomberg School of Public Health. SPF mice were provided and housed by the animal facility of the Johns Hopkins School of Medicine. C57BL/6J, *LysM-cre* [B6.129P2-Lyz2tm1(cre)Ifo/J], and *Myd88*$^{fl/fl}$ [B6.129P2(SJL)-Myd88tm1-Defr/J] mice were obtained from The Jackson Laboratory. *LysM*-cre mice were crossed with MyD88$^{fl/fl}$ mice to obtain the *LysM*-cre × *MyD88*$^{fl/fl}$ mouse strain. *K14-MyD88*$^{-/-}$ mice were provided by N. Archer (Johns Hopkins Medical Institutions). *Il-1*β$^{-/-}$ mice were provided by Y. Iwakura (University of Tokyo) and obtained from the Johns Hopkins University School of Medicine through a material transfer agreement. DNA was extracted from mouse tails to confirm the genotype via PCR. All mouse breeding and experiments were approved by the Johns Hopkins Animal Care and Use Committee and based on Institutional Animal Care and Use Committee protocol MO17M298 (noninfection experiment) and MO25M421 (infection experiment).

Human samples

The human skin samples were acquired according to the Helsinki Principles after volunteers provided informed consent. All study activities were overseen by the Johns Hopkins Institutional Review Board under NA_00033375. Discarded neonatal foreskin from Johns Hopkins Hospital was collected for keratinocyte isolation and culture as described previously (*34*).

Briefly, 32 skin samples from 10 adult volunteers who had not used topical antibiotics within 7 days or systemic antibiotics within 6 months were included. Volunteers were asked not to wash for 24 hours before the start of the study and to refrain from using antibacterial soaps during the study. Twenty-four skin samples from six volunteers were collected for transcriptome sequencing and 16*S* ribosomal RNA (rRNA) sequence (age range: 18 to 53 years old; three males and three females; two Caucasian, one Black, two Hispanic, and one Asian). On day 0 (D0), full-thickness punch biopsies (4 to 5 mm) were obtained from bilateral popliteal fossae. These samples were defined as the unwounded skin (baseline), with the Vaseline and Neosporin groups on the left and right, respectively. After punching, the bilateral popliteal fossa was started with daily medication, one side was treated with Vaseline and the other with Neosporin until healed. Patients 1 to 3 used Neosporin on the left side and Vaseline on the right side,

and patients 4 to 6 used Vaseline on the left side and Neosporin on the right side to rule out the influence of the left and right sides. Volunteers were instructed to use bandages to protect wounds, change dressings, and apply medications daily until healed. The sites were then rebiopsied on D15, and these samples were defined as wounded skin (WD15). Eight skin samples from four volunteers were collected for spatial metabolome mass spectrometry on D15 (age range: 19 to 45 years old; three females and one male; two Caucasian and two Asian). The wounded and unwounded skins of these volunteers were collected and treated as described above.

Human and mouse skin microbiome collection

Six healthy adults with an average age of 28 were included in the skin microbiology study (*1*). Volunteers with skin diseases, infectious diseases, pregnancy, topical antibiotic treatment within 7 days, or systemic antibiotic treatment within 6 months were excluded. All volunteers signed an informed consent form. Participants were asked to refrain from washing for 24 hours before the sample collection, and no antibacterial products were used during the study. The skin microbes were collected from the popliteal fossa on the biopsy day (WD0) and the rebiopsy day (WD15). As mentioned above, the volunteers used Vaseline on one side and Neosporin on the other side every day from WD0 to WD15. A sterile cotton swab (Puritan, 25-1506 1PF TT) premoistened with lysis buffer containing 20 mM tris (pH 8.0; Quality Biological, 723017), 2 mM EDTA (Sigma-Aldrich, E4884), and 1.2% Triton X-100 (Sigma-Aldrich, T9284) was rubbed 40 times at the microbial collection site, covering 6 cm^2. Following the same preparation steps, another swab was waved in the air as a blank control. For mouse skin microbiome collection, we first shaved the back hair with hair clippers. On WD5, we rubbed the skin around the wound 40 times with the swab premoistened in the lysis buffer as described above to collect wound bed microbiome.

WIHN model

All animal experiments were carried out according to our previous WIHN model protocol (*1*, *26*). In short, 21-day-old male and female mice weighing 8 to 12 g with hairs in the first telogen stage were selected. Mice were anesthetized with isoflurane, shaved, and denuded of 1.44 cm^2 full-thickness skin on the lower center of the back, using sterile procedures. The operation day was defined as WD0, and the treatment was performed at WD3 according to each experimental design. At about WD14, the wound scab would fall off. We defined it as scab-detached day (SD0), which is the time point when hair regeneration began. On day 24 after the procedure (WD24), the number of regenerated hair follicles is measured. We visualized the regenerated hair follicles and quantified them using confocal scanning laser microscopy (CLSM), as described before (*26*). In GF mice, we performed the procedure in the bubble of the GF laboratory of the Johns Hopkins School of Public Health. In SPF mice, we performed the procedure in a biological safety hood in the Johns Hopkins School of Medicine. *S. aureus* (1×10^7/50 μl) was injected under the scab on WD3. We also injected 20 μl of 100 nM LW6 (Selleck Chemicals), 1 mM glutamine (Gibco), 200 nM CB839 (Cayman Chemical), 500 nM FX11 (Sigma-Aldrich), or 200 nM UK5099 (Cayman Chemical) under the scab every other day from WD3 to SD0.

Human and mouse keratinocyte isolation, culture, and treatment

Human keratinocytes were obtained from discarded foreskins of male newborns, as described previously (*1*). After the foreskin was cut and laid flat, it was placed in 0.4% sterile dispase II (Sigma-Aldrich, D4693) overnight at 4°C. The next day, sterile forceps were used to separate the epidermis and dermis. The epidermis was subsequently sectioned and digested in trypsin-EDTA (Lonza, CC-5012) for 15 min at 37°C. Trypsin Neutralizing Solution (TNS) (Lonza, CC-5002) was used to terminate the digestion. After filtering the cells through a 6-μm filter and centrifuging them at 2000 rpm for 5 min, we resuspended the keratinocytes in Keratinocyte Growth Medium (KGM) (Lonza, 00192152) and placed them in a humidified, 37°C incubator with 5% CO_2. The medium was changed every other day. Mouse keratinocytes were obtained from male and female newborn mice. After euthanizing six newborn mice and sterilizing them in 75% ethanol, we collected the skin and placed it in 0.4% sterile dispase II (Sigma-Aldrich, D4693) overnight at 4°C. The next day, sterile forceps were used to separate the epidermis from the dermis. Cells were collected as described above for human keratinocytes. All primary keratinocytes were passaged for at least two generations to remove contaminating cells/impurities. Mouse and human keratinocytes were cultured in KGM (Lonza, 00192152) or glutamine-deficient Dulbecco's modified Eagle's medium (Lonza, BE12-614F) and treated with 1×10^7/ml *S. aureus*, 1 mM glutamine (Gibco), 20 nM CB839 (Cayman Chemical), 50 nM FX11 (Sigma-Aldrich), 20 nM UK5099 (Cayman Chemical), or rmIL-1β (100 ng/ml; R&D Systems) according to the design of the different experiments. For the siRNA transfection, we transfected keratinocytes in 12-well plates with 10 nM HIif-1α siRNA or Slc1a7 siRNA (Santa Cruz Biotechnology)–specific or scrambled sequences (Santa Cruz Biotechnology) for 48 hours using Lipofectamine RNA iMAX (Thermo Fisher Scientific). For hypoxia experiments, keratinocytes were cultured in a 2% O_2 incubator at 37°C for 48 hours.

Bacteria strains and preparation

S. aureus (NRS384) was streaked onto trichostatin A (TSA) with a sterile loop. After overnight culture at 37°C, single fluorescent colonies were selected from the plate, inoculated into TSB (BD Bacto, 8330706), and then shaken at 37°C for 18 hours. The bacterial culture was diluted 50-fold with TSB and incubated for another 3 hours to reach the exponential growth period. The bacterial suspension was centrifuged, washed, and resuspended in sterile PBS according to the concentration required for the experiment. Bacteria at the final concentration were plated on TSA or LB and cultured overnight. The number of colony-forming units was determined by absorbance (A600).

Histology, immunofluorescence, and fluorescence microscopy

After obtaining human and mouse skin samples, we flattened them and quickly placed them into 4% paraformaldehyde (PFA; Thermo Fisher Scientific, J19943-K2). After 48 hours of fixation, we submitted the biopsies to the Johns Hopkins University Oncology Tissue Service Core. The biopsies were embedded in paraffin and then sliced into 4-μm-thick sections. The biopsy sections were mounted on glass slides and stained with hematoxylin and eosin (H&E). Biopsy sections were deparaffinized and then used for

antigen retrieval with Target Retrieval Solution. After washing and permeabilizing the sections in TBST [tris-buffered saline (Quality Biological, 351-086-101) containing 0.1% Tween 20 (Sigma-Aldrich, P2287)], we incubated them for 1 hour at room temperature in blocking buffer composed of 5% goat serum and 1% bovine serum albumin (Fisher Bioreagents, BP9703-100). The sections were then incubated overnight at 4°C with the primary antibody dissolved in antibody diluent (Agilent Dako, S0809). The primary antibodies used are as follows: Krt15 (Sigma-Aldrich, HPA023910), active β-catenin (Sigma-Aldrich, 05-665), Il-1β (Abcam, Ab2105), Krt1(Abcam, AB185628), Krt17 (Abcam, ab53707), Cox-2 (Thermo Fisher Scientific, PA5-17614), Col17a1 (Abcam, ab184996), and Ube2c (Abcam, ab252940). After the sections were washed with TBST, we incubated them with fluorescently bound secondary antibody: Alexa Fluor 488 anti-mouse immunoglobulin G (IgG; Invitrogen, A-11001), Alexa Fluor 488 anti-rabbit IgG (Invitrogen, A-11008), and Alexa Fluor 594 anti-rabbit IgG (Invitrogen, A-11037) corresponding to the primary antibody strain for 1 hour at room temperature. Last, after the final TBST washing, cell nuclei were stained with 4′,6-diamidino-2-phenylindole. All slides were imaged using DFC365FX (Leica), and the fluorescence intensity was quantified with ImageJ.

For keratinocyte staining, cells were cultured on sterile cover slides and grown in the incubator until 70% confluent. Cells were then fixed in 4% PFA for 20 min at room temperature, washed with PBS, and incubated in 0.1% Triton X-100 for 15 min at room temperature. Keratinocyte blocking, primary antibody and secondary antibody incubation, and fluorescence intensity quantification were carried out as described above for tissue.

RNA isolation and quantitative real-time PCR

We isolated total RNA from homogenized, freshly collected human and mouse skin and from human and mouse keratinocytes using the RNeasy Mini Kit (Qiagen). The concentration and purity of RNA were determined by microspectrophotometry (NanoDrop2000c, Thermo Fisher Scientific). RNA was reverse-transcribed into complementary DNA with a kit (Applied Biosystems), and the relative expression of the gene of interest was detected by TaqMan probes with FAM dye from Applied Biosystems including murine *Krt15* primers (Mm00492972_m1), murine *Wnt7b* primers (Mm01301717_m1), murine *Krt1* primers (Mm00492992_g1), murine *Krt7* primers (Mm00468876_m1), murine *Hif-1*α primers (Mm00468869_m1), murine *Shh* primers (Mm00436528_m1), murine *Il-1*β primers (Mm00434228_m1), human *KRT1* primers (Hs00196158_m1), and human *KRT15* primers (Hs00856927_g1). Expression levels were compared to those of constitutive genes murine *Rplp0* (Mm00725448_s1), human *RPLP0* (Hs00420895_gH), and murine β-actin (Mm02619580_g1), which were detected by TaqMan probes with VIC dye.

16*S* rRNA gene extraction, PCR amplification, and sequencing

For 16*S* rRNA gene sequencing, human skin microbial samples were sent to CosmoID in Maryland, and mouse skin microbial samples were sent to University of Michigan Medical School, Microbial Systems Molecular Biology Laboratory. Details of 16*S* rRNA gene extraction, PCR amplification, and sequencing have been reported previously (*1*).

Enzyme-linked immunosorbent assay

For each sample, we extracted 20 μg of protein from 1×10^6 keratinocytes after 72 hours of treatment. We also extracted 20 μg of protein from the wound bed of each mouse at WD5. We used commercial assay kits to quantify the expression of glutamate (Abcam, ab83389) and IL-1β (Abcam, ab197742) in cells and tissues.

Mass spectrometry

Mouse and human skin samples were quickly frozen in liquid nitrogen, embedded in unflavored gelatin (Oak Brook, NY), and frozen overnight at −80°C. The next day, a cryostat was used to slice the tissue block into 15-μm sections. The skin sections were adhered to glass slides with an indium tin oxide layer. We used an HTX Imaging M5 TM-Sprayer to apply α-cyano-4-hydroxycinnamic acid (CHCA; 10 mg/ml) matrix to the skin slices. We sprayed the slices six times from top to bottom at 80°C. The spraying capacity of the nozzle was 100 ml/min, and the nozzle was moved at 100 cm/min. We used 2-mm spacing, a spraying pressure of 10 psi, and an air velocity of 3000 ml/min. The distance between the nozzle and the tissue was 4 cm, and the drying time was 20 s. The processed tissue was placed in a vacuum desiccator until being used for MSI analysis.

MALDI MSI

The 15T Solarix FT-ICR (Bruker Daltonics, Billerica, MA) was set to positive ion mode, and the detection mass range was 100 to 800 mass/charge ratio. We set the laser spot to 10 μm and the grating distance to 25 μm. Each pixel was irradiated with 800 continuous lasers, and the matrix α-cyano-4-hydroxycinnamic acid (CHCA), 2,5-dihydroxybenzoic acid (DHB), and lipid standard mixture were used for external calibration on the stainless steel matrix-assisted laser desorption/ionization (MALDI) target. FtmsControl, FlexImaging, and SCiLS Lab were used for image processing. We normalized the spectra of all compounds to count the total ions to reduce the effect of matrix hot spots. Then, we used MSIreader for visualization and relative quantification of the slices. We processed the control group and the treatment group on the same day.

Microarray and bioinformatic analysis

We submitted RNA from the skin of GF mice, SPF mice, *S. aureus*–treated mice, PBS-treated mice, and human popliteal fossae to the Johns Hopkins Deep Sequence Center. The RNA was sequenced by human and murine 1.0ST exon sequencing according to the manufacturer's standard protocol. The original Affymetrix CEL data were standardized using Robust Multichip Analysis (RMA) algorithm for comparison. The data were uploaded to the Gene Expression Omnibus (GEO) under accession numbers GSE158613, GSE158614, and GSE158616.

To calculate the metabolism score, we identified genes of interest in each metabolism pathway from the Kyoto Encyclopedia of Genes and Genomes (KEGG), GSEA-Hallmark, or GO databases and then used the RMA normalization method to convert gene expression of each identified gene to a *z*-score to obtain the relative expression of the two groups of samples as previously described (*54*). The principal components analysis (PCA) algorithm assigns different weighted coefficients according to the contribution of different genes in the metabolism pathway and finally yields the metabolism score by adding the *z*-score of each single gene in the pathway with its

paired coefficient. For the analytic code and introduction of the algorithm, please refer to the GitHub IOBR package (version 0.99.9, date of access 17 June 2021) (https://github.com/IOBR/IOBR) (*55*). Briefly, PCA used the following method to calculate the metabolism score of each sample

$$\text{Metabolism score} = \sum \text{PC1}i - \sum \text{PC1}j$$

In this equation, i is the z-score of the gene whose Cox coefficient is positive, and j is the z-score of the gene whose Cox coefficient is negative. The GSEA analysis was carried out on the GSEA website (http://gsea-msigdb.org/gsea/index.jsp). The relevant biological processes and genes were obtained from KEGG, GSEA, GO, and published literature.

scRNA-seq and bioinformatic analysis

We used R program for scRNA-seq analysis. We generated our self-test dataset GSE190175 and used external WIHN dataset GSE108677. For our in-house mouse data, we obtained two samples (wound center and wound periphery) by pooling tissue from five WT mice for a total 12,760 total cells. We took the scars of mice at SD0 and defined the site of hair follicle regeneration in the center of the wound as the wound center, and the site of non-regenerated hair follicles in wound periphery was defined as the wound periphery. We digested the tissue into single cells and send it to Johns Hopkins Medical Institute (JHMI) Deep Sequencing and Microarray Core to preform 10× single-cell transcriptome sequencing. We analyzed samples from the wound center and wound periphery separately. Seurat package (version 4.0.5) was used to obtain the gene expression matrix for standardized analysis. The t-Distributed Stochastic Neighbor Embedding (t-SNE) function was used to cluster the single cells into five groups based on DEGs according to known specific markers: keratinocytes, fibroblasts, immune cells, endothelial cells, and pericytes. Then, the keratinocytes were clustered into seven subtypes according to published keratinocyte markers: basal1, basal2, basal3, proliferative, spinous, HG, and unknown (*39*). The interactions between different cell types or keratinocyte subtypes were analyzed with R package Cellchat (version 1.1.3) (*56*). Signature genes used to generate the scores were derived from KEGG or gene set variation analysis (GSVA). Hypoxia, metabolism, IL-1 signaling, and keratinocyte differentiation scores were calculated using the PCA method as described above. GO enrichment analysis was carried out with R package Clusterprofiler (version 3.11.1). The pseudotime analysis was carried out with the R package Monocle (version 2.22.0). During the process of WIHN, keratinocytes undergo a transition from one state to another, expressing different sets of genes in different states. The dynamic changes of this expression are transcriptionally regulated, that is, some genes are activated and others are silenced. Monocle learns the dynamics of this gene through a reverse embedding graph algorithm and builds trajectories.

For GSE108677, there are two female mice wound bed tissue pooled in each group, four groups including SWD8, SWD14, large wound day 14 center (LWD14-center), and LWD14-periphery, for a total of eight mice and 15,710 cells. We used nFeature_RNA > 200 and nCount_RNA > 1000 and percent.mt < 20 to screen out high-quality cells and remove exogenous RNA, transfer RNA, and mitochondrial RNA. We used the Seurat package to obtain the gene expression matrix for standardized analysis. Then, we used the t-SNE function to group the single cells into 14 clusters based on DEGs. These 14 clusters were divided into six groups according to the specific cell markers: keratinocytes, endothelial cells, fibroblasts, pericytes, immune cells, and a small number of unknown cells. Hypoxia, metabolism, and IL-1 scores were calculated using the PCA method as described above. Signature genes used to generate the scores were derived from KEGG or GSVA. GO enrichment analysis was performed using R package Clusterprofiler. The R package Monocle was used for pseudotime analysis. The interactions of different cell types were analyzed using R package Cellchat.

To identify DEGs, keratinocytes were separated into two groups: wound center and wound periphery. We used the R package limma to define DEGs among these two groups. To estimate gene expression changes, we implemented an empirical Bayesian approach using moderated t tests. Significance criteria (adjusted P value < 0.05) were used to determine the DEGs among High and Low Glu scores as determined by R package limma. Benjamini-Hochberg correction for multiple testing was used to calculate the adjusted P value. DEGs among keratinocytes from the wound center and periphery were defined using the same method.

Proteomic analysis

Briefly, we collected mouse SD0 scars, divided into wound center and wound periphery, with three mice in each group. We used a commercial protocol to extract skin proteins and used a Waters nanoACQUITY UPLC system and an Orbitrap Fusion Tribrid mass spectrometer for proteomic measurement. The specific processing procedures can be referred to our previous research (*34*). For proteomic analysis, we use the PCA algorithm described above, and we generated metabolism scores based on the expression of metabolic signature genes. Metabolic signature genes were obtained from KEGG, Hallmark, and the published literature.

16*S* rRNA gene sequence bioinformatic analysis

Briefly, we sent the collected skin microbiome to CosmoID in Maryland and University of Michigan Medical School, Microbial Systems Molecular Biology Laboratory for 16*S* rRNA sequencing. Fastx_toolkit_v0.0.14 was used for the raw 16*S* rRNA gene sequencing data analysis, as shown previously (*1*). Based Taxonomic Classification Method (BLCA) and GreenGenes were used for taxonomic classification. QIIME2 was used for operational taxonomic unit analysis and Shannon diversity. α- and β-Diversity was calculated by q2-diversity plugin. The PCA of β-diversity was generated via R package stats cmdscale. Microbiome data were visualized by R package ggplot2.

Statistical analysis

All in vivo and in vitro representative data were from at least three individual substances and two to three independent experiments. Scatterplots and bar graphs are presented as means ± SE. The box plot indicates the minimum, first quartile, median, third quartile, and maximum values. Comparisons between two groups were analyzed by unpaired Student's t test. For multiple-group comparisons, we used one-way analysis of variance (ANOVA) as a parametric method. Statistical significance was defined by P value (*P < 0.05, **P < 0.01, ***P < 0.001, and ****P < 0.0001), and the P values were two-sided. P values less than 0.05 were considered statistically significant. NS indicates no significant difference.

Correlation coefficients were computed by distance correlation and Spearman analyses. To identify significant DEGs, the Benjamini-Hochberg method was applied to convert the *P* values to false discovery rates. All statistical analyses were carried out with R (https://r-project.org/).

Supplementary Materials

This PDF file includes:
Figs. S1 to S7

View/request a protocol for this paper from *Bio-protocol*.

REFERENCES AND NOTES

1. G. Wang, E. Sweren, H. Liu, E. Wier, M. P. Alphonse, R. Chen, N. Islam, A. Li, Y. Xue, J. Chen, Y. Chen, S. Lee, Y. Wang, S. Wang, N. K. Archer, W. Andrews, M. A. Kane, E. Dare, S. K. Reddy, Z. Hu, E. A. Grice, L. S. Miller, L. A. Garza, Bacteria induce skin regeneration via IL-1β signaling. *Cell Host Microbe* **29**, 777–791.e6 (2021).
2. H. Abo, B. Chassaing, A. Harusato, M. Quiros, J. C. Brazil, V. L. Ngo, E. Viennois, D. Merlin, A. T. Gewirtz, A. Nusrat, T. L. Denning, Erythroid differentiation regulator-1 induced by microbiota in early life drives intestinal stem cell proliferation and regeneration. *Nat. Commun.* **11**, 513 (2020).
3. H. Wu, S. Xie, J. Miao, Y. Li, Z. Wang, M. Wang, Q. Yu, *Lactobacillus reuteri* maintains intestinal epithelial regeneration and repairs damaged intestinal mucosa. *Gut Microbes.* **11**, 997–1014 (2020).
4. Y. Liu, Y. Wang, Y. Ni, C. K. Y. Cheung, K. S. L. Lam, Y. Wang, Z. Xia, D. Ye, J. Guo, M. A. Tse, G. Panagiotou, A. Xu, Gut microbiome fermentation determines the efficacy of exercise for diabetes prevention. *Cell Metab.* **31**, 77–91.e5 (2020).
5. J. He, T. Chan, X. Hong, F. Zheng, C. Zhu, L. Yin, W. Dai, D. Tang, D. Liu, Y. Dai, Microbiome and metabolome analyses reveal the disruption of lipid metabolism in systemic lupus erythematosus. *Front. Immunol.* **11**, 1703 (2020).
6. H. Guo, W.-C. Chou, Y. Lai, K. Liang, J. W. Tam, W. J. Brickey, L. Chen, N. D. Montgomery, X. Li, L. M. Bohannon, A. D. Sung, N. J. Chao, J. U. Peled, A. L. C. Gomes, M. R. M. van den Brink, M. J. French, A. N. Macintyre, G. D. Sempowski, X. Tan, R. Balfour Sartor, K. Lu, J. P. Y. Ting, Multi-omics analyses of radiation survivors identify radioprotective microbes and metabolites. *Science* **370**, eaay9097 (2020).
7. P. Kundu, H. U. Lee, I. Garcia-Perez, E. X. Y. Tay, H. Kim, L. E. Faylon, K. A. Martin, R. Purbojati, D. I. Drautz-Moses, S. Ghosh, J. K. Nicholson, S. Schuster, E. Holmes, S. Pettersson, Neurogenesis and prolongevity signaling in young germ-free mice transplanted with the gut microbiota of old mice. *Sci. Transl. Med.* **11**, eaau4760 (2019).
8. P.-F. Roux, T. Oddos, G. Stamatas, Deciphering the role of skin surface microbiome in skin health: An integrative multiomics approach reveals three distinct metabolite-microbe clusters. *J. Invest. Dermatol.* **142**, 469–479.e5 (2021).
9. D. Chen, J. He, J. Li, Q. Zou, J. Si, Y. Guo, J. Yu, C. Li, F. Wang, T. Chan, H. Shi, Microbiome and metabolome analyses reveal novel interplay between the skin microbiota and plasma metabolites in psoriasis. *Front. Microbiol.* **12**, 643449 (2021).
10. Y. Cai, F. Xue, C. Quan, M. Qu, N. Liu, Y. Zhang, C. Fleming, X. Hu, H. G. Zhang, R. Weichselbaum, Y. X. Fu, D. Tieri, E. C. Rouchka, J. Zheng, J. Yan, A critical role of the IL-1β–IL-1R signaling pathway in skin inflammation and psoriasis pathogenesis. *J. Invest. Dermatol.* **139**, 146–156 (2018).
11. R. M. Salgado, L. Alcántara, C. A. Mendoza-Rodríguez, M. Cerbón, C. Hidalgo-González, P. Mercadillo, L. M. Moreno, R. Alvarez-Jiménez, E. Krötzsch, Post-burn hypertrophic scars are characterized by high levels of IL-1β mRNA and protein and TNF-α type I receptors. *Burns* **38**, 668–676 (2012).
12. A. E. Rodriguez, G. S. Ducker, L. K. Billingham, C. A. Martinez, N. Mainolfi, V. Suri, A. Friedman, M. G. Manfredi, S. E. Weinberg, J. D. Rabinowitz, N. S. Chandel, Serine metabolism supports macrophage IL-1β production. *Cell Metab.* **29**, 1003–1011.e4 (2019).
13. G. M. Tannahill, A. M. Curtis, J. Adamik, E. M. Palsson-McDermott, A. F. McGettrick, G. Goel, C. Frezza, N. J. Bernard, B. Kelly, N. H. Foley, L. Zheng, A. Gardet, Z. Tong, S. S. Jany, S. C. Corr, M. Haneklaus, B. E. Caffrey, K. Pierce, S. Walmsley, F. C. Beasley, E. Cummins, V. Nizet, M. Whyte, C. T. Taylor, H. Lin, S. L. Masters, E. Gottlieb, V. P. Kelly, C. Clish, P. E. Auron, R. J. Xavier, L. A. O'Neill, Succinate is an inflammatory signal that induces IL-1β through HIF-1α. *Nature* **496**, 238–242 (2013).
14. C. S. Kim, X. Ding, K. Allmeroth, L. C. Biggs, O. I. Kolenc, N. L'Hoest, C. A. Chacón-Martínez, C. Edlich-Muth, P. Giavalisco, K. P. Quinn, M. S. Denzel, S. A. Eming, S. A. Wickström, Glutamine metabolism controls stem cell fate reversibility and long-term maintenance in the hair follicle. *Cell Metab.* **32**, 629–642.e8 (2020).
15. R. Williams, M. P. Philpott, T. Kealey, Metabolism of freshly isolated human hair follicles capable of hair elongation: A glutaminolytic, aerobic glycolytic tissue. *J. Invest. Dermatol.* **100**, 834–840 (1993).
16. R. Raizel, J. S. M. Leite, T. M. Hypólito, A. Y. Coqueiro, P. Newsholme, V. F. Cruzat, J. Tirapegui, Determination of the anti-inflammatory and cytoprotective effects of L-glutamine and L-alanine, or dipeptide, supplementation in rats submitted to resistance exercise. *Br. J. Nutr.* **116**, 470–479 (2016).
17. Y. Shi, Z. Tu, D. Tang, H. Zhang, M. Liu, K. Wang, S. K. Calderwood, X. Xiao, The inhibition of LPS-induced production of inflammatory cytokines by HSP70 involves inactivation of the NF-κB pathway but not the MAPK pathways. *Shock* **26**, 277–284 (2006).
18. H. Charles-Messance, G. Blot, A. Couturier, L. Vignaud, S. Touhami, F. Beguier, L. Siqueiros, V. Forster, N. Barmo, S. Augustin, S. Picaud, J. A. Sahel, A. Rendon, A. Grosche, R. Tadayoni, F. Sennlaub, X. Guillonneau, IL-1β induces rod degeneration through the disruption of retinal glutamate homeostasis. *J. Neuroinflammation* **17**, 1 (2020).
19. M. Wickersham, S. Wachtel, T. W. F. Lung, G. Soong, R. Jacquet, A. Richardson, D. Parker, A. Prince, Metabolic stress drives keratinocyte defenses against *Staphylococcus aureus* infection. *Cell Rep.* **18**, 2742–2751 (2017).
20. A. F. McGettrick, L. A. J. O'Neill, The role of HIF in immunity and inflammation. *Cell Metab.* **32**, 524–536 (2020).
21. J. W. Kim, I. Tchernyshyov, G. L. Semenza, C. V. Dang, HIF-1-mediated expression of pyruvate dehydrogenase kinase: A metabolic switch required for cellular adaptation to hypoxia. *Cell Metab.* **3**, 177–185 (2006).
22. E. Schipani, H. E. Ryan, S. Didrickson, T. Kobayashi, M. Knight, R. S. Johnson, Hypoxia in cartilage: HIF-1alpha is essential for chondrocyte growth arrest and survival. *Genes Dev.* **15**, 2865–2876 (2001).
23. O. Genbacev, Y. Zhou, J. W. Ludlow, S. J. Fisher, Regulation of human placental development by oxygen tension. *Science* **277**, 1669–1672 (1997).
24. A. Flores, J. Schell, A. S. Krall, D. Jelinek, M. Miranda, M. Grigorian, D. Braas, A. C. White, J. L. Zhou, N. A. Graham, T. Graeber, P. Seth, D. Evseenko, H. A. Coller, J. Rutter, H. R. Christofk, W. E. Lowry, Lactate dehydrogenase activity drives hair follicle stem cell activation. *Nat. Cell Biol.* **19**, 1017–1026 (2017).
25. A. G. Lone, E. Atci, R. Renslow, H. Beyenal, S. Noh, B. Fransson, N. Abu-Lail, J. J. Park, D. R. Gang, D. R. Call, Staphylococcus aureus induces hypoxia and cellular damage in porcine dermal explants. *Infect. Immun.* **83**, 2531–2541 (2015).
26. A. M. Nelson, S. K. Reddy, T. S. Ratliff, M. Z. Hossain, A. S. Katseff, A. S. Zhu, E. Chang, S. R. Resnik, C. Page, D. Kim, A. J. Whittam, L. S. Miller, L. A. Garza, dsRNA released by tissue damage activates TLR3 to drive skin regeneration. *Cell Stem Cell* **17**, 139–151 (2015).
27. W. A. Boisvert, M. Yu, Y. Choi, G. H. Jeong, Y. L. Zhang, S. Cho, C. Choi, S. Lee, B. H. Lee, Hair growth-promoting effect of Geranium sibiricum extract in human dermal papilla cells and C57BL/6 mice. *BMC Complement. Altern. Med.* **17**, 109 (2017).
28. M. Chai, M. Jiang, L. Vergnes, X. Fu, S. C. de Barros, N. B. Doan, W. Huang, J. Chu, J. Jiao, H. Herschman, G. M. Crooks, K. Reue, J. Huang, Stimulation of hair growth by small molecules that activate autophagy. *Cell Rep.* **27**, 3413–3421.e3 (2019).
29. K. Allmeroth, C. S. Kim, A. Annibal, A. Pouikli, J. Koester, M. J. Derisbourg, C. Andres Chacon-Martinez, C. Latza, A. Antebi, P. Tessarz, S. A. Wickstrom, M. S. Denzel, *N*1-acetylspermidine is a determinant of hair follicle stem cell fate. *J. Cell Sci.* **134**, jcs252767 (2021).
30. S. Park, W. Kang, D. Choi, B. Son, T. Park, Nonanal stimulates growth factors via cyclic adenosine monophosphate (cAMP) signaling in human hair follicle dermal papilla cells. *Int. J. Mol. Sci.* **21**, 8054 (2020).
31. G. Biolo, G. Toigo, B. Ciocchi, R. Situlin, F. Iscra, A. Gullo, G. Guarnieri, Metabolic response to injury and sepsis: Changes in protein metabolism. *Nutrition* **13**, 52S–57S (1997).
32. U. Kesici, S. Kesici, H. Ulusoy, F. Yucesan, A. U. Turkmen, A. Besir, V. Tuna, Effects of glutamine on wound healing. *Int. Wound J.* **12**, 280–284 (2015).
33. N. K. Archer, J. H. Jo, S. K. Lee, D. Kim, B. Smith, R. V. Ortines, Y. Wang, M. C. Marchitto, A. Ravipati, S. S. Cai, C. A. Dillen, H. Liu, R. J. Miller, A. G. Ashbaugh, A. S. Uppal, M. K. Oyoshi, N. Malhotra, S. Hoff, L. A. Garza, H. H. Kong, J. A. Segre, R. S. Geha, L. S. Miller, Injury, dysbiosis, and filaggrin deficiency drive skin inflammation through keratinocyte IL-1α release. *J. Allergy Clin. Immunol.* **143**, 1426–1443.e6 (2019).
34. D. Kim, R. Chen, M. Sheu, N. Kim, S. Kim, N. Islam, E. M. Wier, G. Wang, A. Li, A. Park, W. Son, B. Evans, V. Yu, V. P. Prizmic, E. Oh, Z. Wang, J. Yu, W. Huang, N. K. Archer, Z. Hu, N. Clemetson, A. M. Nelson, A. Chien, G. A. Okoye, L. S. Miller, G. Ghiaur, S. Kang, J. W. Jones, M. A. Kane, L. A. Garza, Noncoding dsRNA induces retinoic acid synthesis to stimulate hair follicle regeneration via TLR3. *Nat. Commun.* **10**, 2811 (2019).
35. S. Stegen, N. van Gastel, G. Eelen, B. Ghesquiere, F. D'Anna, B. Thienpont, J. Goveia, S. Torrekens, R. Van Looveren, F. P. Luyten, P. H. Maxwell, B. Wielockx, D. Lambrechts, S. M. Fendt, P. Carmeliet, G. Carmeliet, HIF-1α promotes glutamine-mediated redox homeostasis and glycogen-dependent bioenergetics to support postimplantation bone cell survival. *Cell Metab.* **23**, 265–279 (2016).

36. R. C. Sun, N. C. Denko, Hypoxic regulation of glutamine metabolism through HIF1 and SIAH2 supports lipid synthesis that is necessary for tumor growth. *Cell Metab.* **19**, 285–292 (2014).
37. Y. Kanai, B. Clemencon, A. Simonin, M. Leuenberger, M. Lochner, M. Weisstanner, M. A. Hediger, The SLC1 high-affinity glutamate and neutral amino acid transporter family. *Mol. Aspects Med.* **34**, 108–120 (2013).
38. S. Abbasi, S. Sinha, E. Labit, N. L. Rosin, G. Yoon, W. Rahmani, A. Jaffer, N. Sharma, A. Hagner, P. Shah, R. Arora, J. Yoon, A. Islam, A. Uchida, C. K. Chang, J. A. Stratton, R. W. Scott, F. M. V. Rossi, T. M. Underhill, J. Biernaskie, Distinct regulatory programs control the latent regenerative potential of dermal fibroblasts during wound healing. *Cell Stem Cell* **27**, 396–412.e6 (2020).
39. D. Haensel, S. Jin, P. Sun, R. Cinco, M. Dragan, Q. Nguyen, Z. Cang, Y. Gong, R. Vu, A. L. MacLean, K. Kessenbrock, E. Gratton, Q. Nie, X. Dai, Defining epidermal basal cell states during skin homeostasis and wound healing using single-cell transcriptomics. *Cell Rep.* **30**, 3932–3947.e6 (2020).
40. D. Gay, O. Kwon, Z. Zhang, M. Spata, M. V. Plikus, P. D. Holler, M. Ito, Z. Yang, E. Treffeisen, C. D. Kim, A. Nace, X. Zhang, S. Baratono, F. Wang, D. M. Ornitz, S. E. Millar, G. Cotsarelis, Fgf9 from dermal γδ T cells induces hair follicle neogenesis after wounding. *Nat. Med.* **19**, 916–923 (2013).
41. M. Ito, Z. Yang, T. Andl, C. Cui, N. Kim, S. E. Millar, G. Cotsarelis, Wnt-dependent de novo hair follicle regeneration in adult mouse skin after wounding. *Nature* **447**, 316–320 (2007).
42. A. Mohyeldin, T. Garzon-Muvdi, A. Quinones-Hinojosa, Oxygen in stem cell biology: A critical component of the stem cell niche. *Cell Stem Cell* **7**, 150–161 (2010).
43. M. Ito, Y. Liu, Z. Yang, J. Nguyen, F. Liang, R. J. Morris, G. Cotsarelis, Stem cells in the hair follicle bulge contribute to wound repair but not to homeostasis of the epidermis. *Nat. Med.* **11**, 1351–1354 (2005).
44. J. Zhang, X. C. He, W. G. Tong, T. Johnson, L. M. Wiedemann, Y. Mishina, J. Q. Feng, L. Li, Bone morphogenetic protein signaling inhibits hair follicle anagen induction by restricting epithelial stem/progenitor cell activation and expansion. *Stem Cells* **24**, 2826–2839 (2006).
45. S. Joost, A. Zeisel, T. Jacob, X. Sun, G. La Manno, P. Lonnerberg, S. Linnarsson, M. Kasper, Single-cell transcriptomics reveals that differentiation and spatial signatures shape epidermal and hair follicle heterogeneity. *Cell Syst.* **3**, 221–237.e9 (2016).
46. P. G. Noleto, J. P. E. Saut, I. M. Sheldon, Short communication: Glutamine modulates inflammatory responses to lipopolysaccharide in ex vivo bovine endometrium. *J. Dairy Sci.* **100**, 2207–2212 (2017).
47. K. Ren, R. Dubner, Interactions between the immune and nervous systems in pain. *Nat. Med.* **16**, 1267–1276 (2010).
48. E. D. Milligan, L. R. Watkins, Pathological and protective roles of glia in chronic pain. *Nat. Rev. Neurosci.* **10**, 23–36 (2009).
49. D. C. C. Healey, J. Y. Cephus, S. M. Barone, N. U. Chowdhury, D. O. Dahunsi, M. Z. Madden, X. Ye, X. Yu, K. Olszewski, K. Young, V. A. Gerriets, P. J. Siska, R. Dworski, J. Hemler, J. W. Locasale, M. V. Poyurovsky, R. S. Peebles Jr., J. M. Irish, D. C. Newcomb, J. C. Rathmell, Targeting in vivo metabolic vulnerabilities of T_H2 and T_H17 cells reduces airway inflammation. *J. Immunol.* **206**, 1127–1139 (2021).
50. G. Gao, C. Li, J. Zhu, Y. Wang, Y. Huang, S. Zhao, S. Sheng, Y. Song, C. Ji, C. Li, X. Yang, L. Ye, X. Qi, Y. Zhang, X. Xia, J. C. Zheng, Glutaminase 1 regulates neuroinflammation after cerebral ischemia through enhancing microglial activation and pro-inflammatory exosome release. *Front. Immunol.* **11**, 161 (2020).
51. H. Morinaga, Y. Mohri, M. Grachtchouk, K. Asakawa, H. Matsumura, M. Oshima, N. Takayama, T. Kato, Y. Nishimori, Y. Sorimachi, K. Takubo, T. Suganami, A. Iwama, Y. Iwakura, A. A. Dlugosz, E. K. Nishimura, Obesity accelerates hair thinning by stem cell-centric converging mechanisms. *Nature* **595**, 266–271 (2021).
52. P. Lee, R. Gund, A. Dutta, N. Pincha, I. Rana, S. Ghosh, D. Witherden, E. Kandyba, A. MacLeod, K. Kobielak, W. L. Havran, C. Jamora, Stimulation of hair follicle stem cell proliferation through an IL-1 dependent activation of γδT-cells. *eLife* **6**, e28875 (2017).
53. L. Gong, J. Xiao, X. Li, Y. Li, X. Gao, X. Xu, IL-36α promoted wound induced hair follicle neogenesis via hair follicle stem/progenitor cell proliferation. *Front. Cell Dev. Biol.* **8**, 627 (2020).
54. G. Wang, Y. Miao, N. Kim, E. Sweren, S. Kang, Z. Hu, L. A. Garza, Association of the psoriatic microenvironment with treatment response. *JAMA Dermatol.* **156**, 1057–1065 (2020).
55. D. Zeng, Z. Ye, R. Shen, G. Yu, J. Wu, Y. Xiong, R. Zhou, W. Qiu, N. Huang, L. Sun, X. Li, J. Bin, Y. Liao, M. Shi, W. Liao, IOBR: Multi-omics immuno-oncology biological research to decode tumor microenvironment and signatures. *Front. Immunol.* **12**, 687975 (2021).
56. S. Jin, C. F. Guerrero-Juarez, L. Zhang, I. Chang, R. Ramos, C. H. Kuan, P. Myung, M. V. Plikus, Q. Nie, Inference and analysis of cell-cell communication using CellChat. *Nat. Commun.* **12**, 1088 (2021).

Acknowledgments: We thank the Chinese Skin Microbiome (CSM) Study Group at the Department of Plastic and Aesthetic Surgery, Nanfang Hospital, for technical support and the Cutaneous Translational Research Program (CTReP) in the Department of Dermatology, Johns Hopkins Hospital for organizing human subjects and preparing tissue samples. We also thank G. Semenza and C. Levine for feedback on the project and manuscript, respectively, and the Guangdong Provincial Key Laboratory of Construction and Detection in Tissue Engineering for providing experimental instruments. **Funding:** This work was supported by the National Institute of Arthritis and Musculoskeletal and Skin Diseases, part of the National Institutes of Health, under R01AR074846 01 and UG3 AR079376 to L.A.G.; the Thomas Provost, MD, Young Faculty Development Fund of Johns Hopkins Dermatology to L.A.G.; and the National Natural Science Foundation of China (grant no. 82202468) to G.W. **Author contributions:** Conceptualization: G.W. and L.A.G. Methodology: G.W., E.S., W.A., M.A.K., and J.C. Investigation: G.W., Y.L., Y.X., E.W., M.P.A., L.L., Y.M., R.C., D.Z., S.L., A.L., E.D., D.K., N.K.A., and L.R. Visualization: G.W., W.A., and J.C. Supervision: Z.H., M.A.K., E.A.G., S.K.R., and L.A.G. Writing—original draft: G.W. Writing—review and editing: E.A.S., S.K.R., and L.A.G. **Competing interests:** The authors declare that they have no competing interests. **Data and materials availability:** All data needed to evaluate the conclusions in the paper are present in the paper and/or the Supplementary Materials. The microarray data were deposited in the NCBI GEO: https://ncbi.nlm.nih.gov/geo/ under accession numbers GSE158613, GSE158614, and GSE158616. The 16*S* rRNA-seq data were deposited in NCBI Sequenced Read Archive (SRA): https://ncbi.nlm.nih.gov/sra/?term= under accession numbers PRJNA665993 and PRJNA665992. The scRNA-seq data were deposited in the NCBI GEO under accession number GSE190175. The public scRNA-seq data were obtained from GEO under GSE108677.

Submitted 23 February 2022
Accepted 23 November 2022
Published 4 January 2023
10.1126/sciadv.abo7555